Geophysical Journal International

Geophys. J. Int. (2016) **206,** 241–259
Advance Access publication 2016 April 15
GJI Seismology

doi: 10.1093/gji/ggw151

Imaging Rayleigh wave attenuation with USArray

Xueyang Bao,[1,*] Colleen A. Dalton,[1] Ge Jin,[2] James B. Gaherty[2] and Yang Shen[3]

[1]*Earth, Environmental and Planetary Sciences, Brown University,* 324 *Brook Street, Providence RI* 02912*, USA. E-mail:* xybao@uri.edu
[2]*Lamont-Doherty Earth Observatory of Columbia University,* 61 *Route* 9 *W, Palisades, NY* 10964*, USA*
[3]*Graduate School of Oceanography, University of Rhode Island,* 215 *South Ferry Road, Narragansett, RI* 02882*, USA*

Accepted 2016 April 13. Received 2016 April 12; in original form 2015 July 3

SUMMARY

The EarthScope USArray provides an opportunity to obtain detailed images of the continental upper mantle at an unprecedented scale. The majority of mantle models derived from USArray data to date contain spatial variations in seismic-wave speed; however, in many cases these data sets do not by themselves allow a non-unique interpretation. Joint interpretation of seismic attenuation and velocity models can improve upon the interpretations based only on velocity and provide important constraints on the temperature, composition, melt content, and volatile content of the mantle. The surface wave amplitudes that constrain upper-mantle attenuation are sensitive to factors in addition to attenuation, including the earthquake source excitation, focusing and defocusing by elastic structure, and local site amplification. Because of the difficulty of isolating attenuation from these other factors, little is known about the attenuation structure of the North American upper mantle. In this study, Rayleigh wave traveltime and amplitude in the period range 25–100 s are measured using an interstation cross-correlation technique, which takes advantage of waveform similarity at nearby stations. Several estimates of Rayleigh wave attenuation and site amplification are generated at each period, using different approaches to separate the effects of attenuation and local site amplification on amplitude. It is assumed that focusing and defocusing effects can be described by the Laplacian of the traveltime field. All approaches identify the same large-scale patterns in attenuation, including areas where the attenuation values are likely contaminated by unmodelled focusing and defocusing effects. Regionally averaged attenuation maps are constructed after removal of the contaminated attenuation values, and the variations in intrinsic shear attenuation that are suggested by these Rayleigh wave attenuation maps are explored.

Key words: Surface waves and free oscillations; Seismic attenuation; Site effects; North America.

1 INTRODUCTION

Seismic attenuation ($1/Q$) offers complementary constraints on the physical and chemical state of the mantle relative to those provided by shear velocity. Jointly interpreting attenuation and velocity models should help reduce ambiguity in the traditional interpretation of wave speeds (e.g. Roth *et al*. 2000; Yang *et al*. 2007; Dalton *et al*. 2009; Zhu *et al*. 2013). For example, increased temperature at fixed pressure leads to higher attenuation and reduced shear velocity, with attenuation exhibiting very strong sensitivity to high temperatures (Anderson 1967; Sato *et al.* 1989; Karato 1993; Goes *et al.* 2000; Jackson *et al.* 2002). On the other hand, attenuation is expected to be less sensitive to major-element compositional variations than velocity (Faul & Jackson 2005; Shito *et al.* 2006; Wiens *et al.* 2008), although there is little experimental data to support this assumption. Partial melt has been shown to reduce velocities and increase attenuation; the details of this effect depend on the mechanism (Hammond & Humphreys 2000a,b; Faul *et al.* 2004). Finally, it is expected that water will strongly enhance attenuation and indirectly influence velocity through anelastic dispersion (Karato & Jung 1998; Karato 2003). Recent laboratory measurements of shear modulus and attenuation in olivine (Gribb & Cooper 1998; Jackson *et al.* 2002; Faul *et al.* 2004; Jackson & Faul 2010) and polyphase samples (Sundberg & Cooper 2010), made at seismic frequencies, high temperatures, and with variable degrees of partial melt, are beginning to provide valuable quantitative constraints with which to interpret regional and global seismic models (e.g. Faul & Jackson 2005; Yang *et al.* 2007; Dalton & Faul 2010; Abers *et al.* 2014; Wei *et al.* 2015).

*Now at: Graduate School of Oceanography, University of Rhode Island, 215 South Ferry Road, Narragansett, RI 02882, USA.

Anelasticity also causes a frequency dependence of seismic velocity, with lower wave speeds at lower frequencies (e.g. Liu *et al.* 1976; Kanamori & Anderson 1977). An important consequence of this phenomenon is that the temperatures inferred from shear velocity will depend on assumptions about anelastic properties (e.g. Jackson *et al.* 2004; Shapiro & Ritzwoller 2004). As an example, reduction in shear velocity from 4.65 to 4.40 km s^{-1} at 100-km depth corresponds to a temperature increase of $\sim$600 $^{\circ}$C for a purely elastic calculation (e.g. Stixrude & Lithgow-Bertelloni 2005) and $\sim$400 $^{\circ}$C using the anelastic model of Faul & Jackson (2005) with a grain size of 5 cm. Anelastic dispersion also affects conclusions drawn about partial melting in two ways. One, if a smaller maximum temperature is inferred when anelasticity is considered, as in the above example, the likelihood of melting is reduced. Two, if melt is present, the range of temperatures is even smaller than for the melt-free case (e.g. Jackson *et al.* 2004) because part of the velocity reduction can be attributed to the presence of melt. Thus, models of mantle attenuation are valuable not only because they provide constraints on mantle structure that are complementary to wave-speed models but also because they are critical in order to achieve an accurate interpretation of velocity variations.

Attenuation tomography has historically lagged behind velocity tomography and been a less successful means of probing the Earth's interior. This is apparent from the relatively small number of global and regional attenuation studies performed to date and is not surprising, given that the wave amplitude, which is the primary observable in attenuation studies, requires a more complex interpretation than wave phase. In addition to intrinsic attenuation, amplitudes are affected by propagation through elastic heterogeneity (focusing/defocusing due to spatial gradients in wave speed as well as scattering effects), uncertainties in the estimation of earthquake source excitation, and site amplification and errors in instrument calibration at the receiver. In order to isolate the signal of anelastic decay in the amplitude data, these extraneous effects must somehow be accounted for.

For the intermediate-period Rayleigh waves utilized in this study, focusing effects are especially important. The focusing effect on amplitude depends on the phase-velocity gradient perpendicular to the propagation path, causing amplitudes to be strongly sensitive to short-wavelength elastic structure and to errors in the assumed propagation path (Woodhouse & Wong 1986; Wang & Dahlen 1994; Wang & Dahlen 1995; Larson *et al.* 1998; Dalton *et al.* 2013). While amplitudes' sensitivity to elastic structure presents an opportunity for improving images of velocity structure (e.g. Dunn & Forsyth 2003; Dalton & Ekström 2006b; Yang & Forsyth 2006; Lin & Ritzwoller 2011), it presents a challenge for imaging attenuation structure. Several studies have documented ways in which unmodelled focusing effects can introduce artefacts into attenuation models (Selby & Woodhouse 2000; Dalton & Ekström 2006a; Ruan & Zhou 2012). Despite these difficulties, there has been considerable recent progress in our ability to image upper-mantle attenuation and draw inferences about the physical and chemical state of the upper mantle (e.g. Romanowicz & Gung 2002; Gung & Romanowicz 2004; Stachnik *et al.* 2004; Yang *et al.* 2007; Dalton *et al.* 2008; Rychert *et al.* 2008; Yang & Forsyth 2008; Zhu *et al.* 2013; Abers *et al.* 2014; Booth *et al.* 2014).

Only a handful of studies have focused on attenuation within the North American upper mantle, and they primarily have in common the first-order pattern of high attenuation beneath tectonically active western North America and low attenuation beneath tectonically stable eastern North America (e.g. Mitchell 1975; Lay & Helmberger 1981; Lawrence *et al.* 2006; Hwang *et al.* 2009). On smaller-scale features agreement between various studies is generally weak. While there have also been attenuation studies focused on particular regions within North America, for example Southern California (Yang & Forsyth 2008), the Basin and Range and Pacific Northwest (Lay & Wallace 1988), and the western United States (Lin *et al.* 2012), a continental-scale mantle attenuation model for North America derived from surface waves has not previously been constructed.

The data collected by the EarthScope USArray over the past decade provide a unique opportunity to image upper-mantle attenuation beneath North America at a scale not previously possible. In this study, we utilize Rayleigh wave traveltimes and amplitudes measured at periods between 25 and 100 s to construct 2-D phase-velocity and attenuation maps across the continent. We follow the Helmholtz tomography theory and approach outlined by Lin *et al.* (2012), and use three approaches to separate the effects of attenuation and local site amplification on the amplitudes. We investigate possible bias introduced into the attenuation maps by imperfect treatment of focusing effects and, after eliminating attenuation values that we suspect are unreliable, present regionally averaged Rayleigh wave attenuation maps at several periods. The range of mantle shear-attenuation ($Q_{\mu}{}^{-1}$) values that are suggested by the 2-D maps is also explored.

2 SURFACE WAVE MEASUREMENTS

Measurements of fundamental-mode Rayleigh wave amplitude and phase are determined using cross-correlation of waveforms at nearby stations (Jin & Gaherty 2015). This approach, which is built upon the Generalized Seismological Data Functional (GSDF) analysis of Gee & Jordan (1992), takes advantage of the similarity of waveforms recorded at nearby stations to obtain precise estimates of the relative phase delay between pairs of stations. The measurement procedure, called the Automated Surface Wave Phase Velocity Measuring System (ASWMS) and described in detail by Jin & Gaherty (2015), is available as a data product from the Incorporated Research Institutions for Seismology (IRIS).

This study utilizes both amplitude and phase. The raw phase measurements are, for each event, measurements of the time lag between two stations i and j. We convert these interstation delay times $\delta\tau_{\mathrm{ij}}$ into single-station delay times τ_{i} by specifying, for each event, the delay time at a reference station (e.g. $\tau_1 = 0$ s) and then determining the delay times at all other stations using least-squares inversion. Since only relative and not absolute traveltimes are needed to obtain the phase-velocity and attenuation maps, the results do not depend on which station is assigned as the reference station or what is the value of the delay time at the reference station. The amplitude measurements A_{i} are single-station measurements. ASWMS applies a five-parameter wavelet fitting to the windowed and narrow-band-filtered auto-correlation function calculated for the waveform at each station. The five-parameter wavelet is defined as $\tilde{A}\,\mathrm{Ga}[\tilde{\sigma}(t - \tilde{t}_g)]\cos[\tilde{\omega}(t - \tilde{t}_p)]$, where $\tilde{t}_g$ and $\tilde{t}_p$ are the frequency-dependent group and phase delay, respectively, Ga is the Gaussian function, $\tilde{A}$ is a positive scaling factor, $\tilde{\sigma}$ is the half-bandwidth, and $\tilde{\omega}$ is the centre frequency of the narrow-band waveform. We use $\tilde{A}$ to approximate the power spectrum density function at the centre frequency of narrow-band filter, and thus the amplitude A_{i} is measured from the square root of $\tilde{A}$ (Jin & Gaherty 2015). The width of the filter is approximately 10 per cent of the centre frequency.

We use the following approach to identify and eliminate obvious outliers in the amplitude data. For each event, the median amplitudes

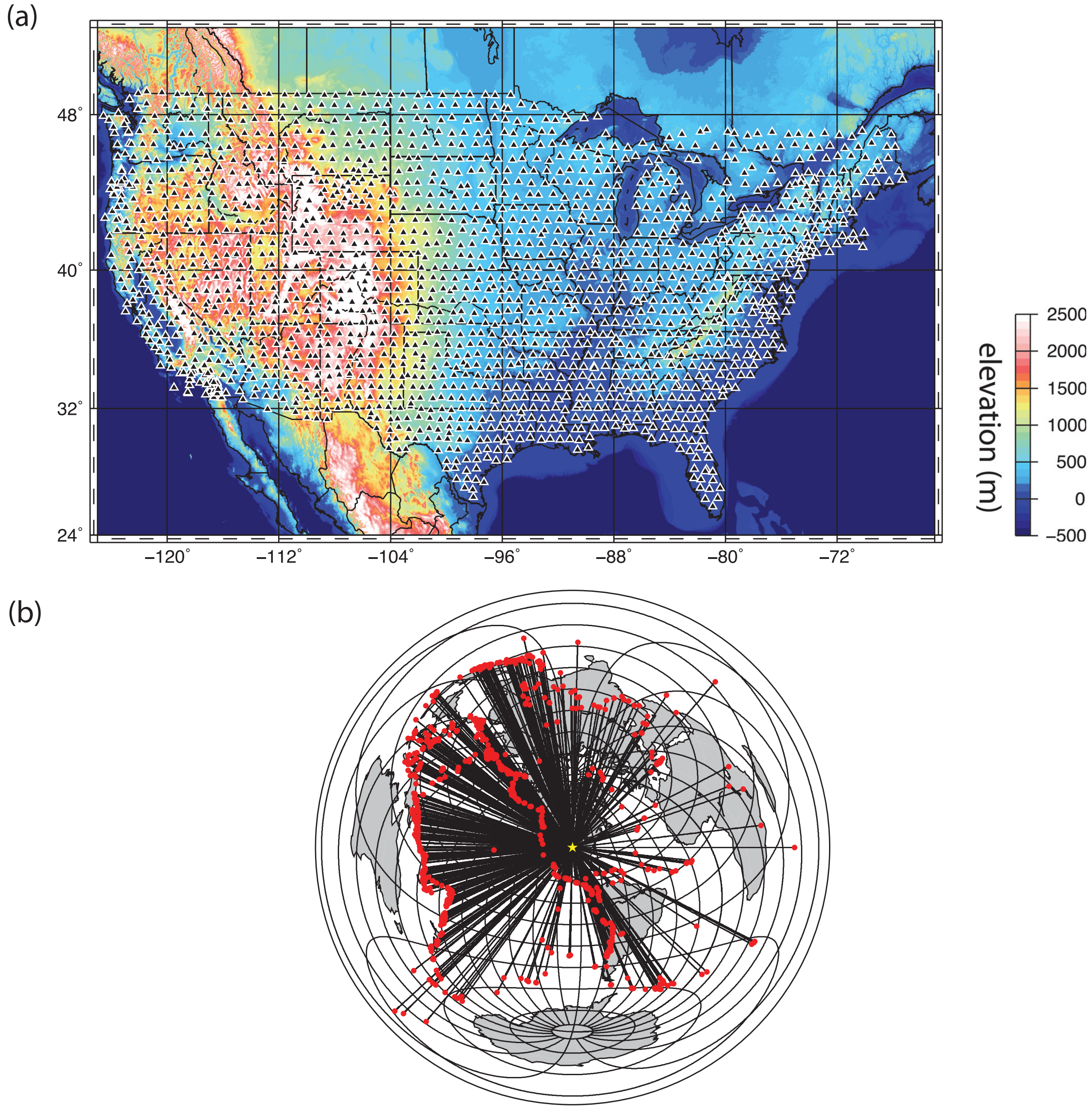

Figure 1. (a) Map of study area. Triangles represent seismic stations that contributed data. The colour scale shows surface topography. (b) Map of earthquakes that contributed data (red circles). The yellow star, at the location of the station Q36A in Lecompton, Kansas, approximates the centre of the study area. Black lines indicate great-circle paths connecting each earthquake with the yellow star.

of groups of stations located within a 200-km radius of each other are determined. If the amplitude measured at an individual station exceeds ±50 per cent of the median value of the station group to which that station belongs, the measurement is rejected. Since the amplitude measurements are not made with respect to a reference synthetic seismogram, they contain the effects of the earthquake source, propagation (attenuation, focusing and scattering), and local site amplification. In Section 3, we describe the approaches we utilize to isolate the signal of attenuation in the amplitude data.

The total data set includes 882 teleseismic (epicentral distances between 20° and 160°) earthquakes with $M_w > 6.0$ and depth <50 km that occurred between 2006 January 2 and 2015 March 3 and 1966 seismic stations. The initial data set, before selection, has 389 552 amplitude and traveltime measurements at each period. Fig. 1 shows the station and event locations and summarizes the azimuthal distribution of events.

3 METHODS

3.1 Theoretical background

The theoretical basis for the approach followed in this study was developed and described by Lin *et al.* (2012) and Lin & Ritzwoller (2011). Here we summarize the key equations. The single-frequency single-mode 2-D surface wave potential $\chi_{2D}(\mathbf{r}, t)$ can be related to the phase traveltime $\tau(\mathbf{r})$ and amplitude $A(\mathbf{r})$, which are observed at position $\mathbf{r}$ on the 2-D surface, at time t such that

$$\chi_{2D}(\mathbf{r}, t) = \frac{A(\mathbf{r})}{\beta(\mathbf{r})} \exp\left\{i\omega\left[t - \tau(\mathbf{r})\right]\right\}, \tag{1}$$

where ω is angular frequency and $\beta(\mathbf{r})$ is the local site amplification. The 2-D surface wave potential approximately satisfies the 2-D homogeneous damped wave equation

$$\frac{1}{c(\mathbf{r})^2}\frac{\partial^2\chi_{2D}(\mathbf{r}, t)}{\partial t^2} = -\frac{2\alpha(\mathbf{r})}{c(\mathbf{r})}\frac{\partial\chi_{2D}(\mathbf{r}, t)}{\partial t} + \nabla^2\chi_{2D}(\mathbf{r}, t), \tag{2}$$

where $c(\mathbf{r})$ is phase velocity and $\alpha(\mathbf{r})$ is the attenuation coefficient, which is related to Rayleigh wave attenuation Q^{-1} by $\alpha = \omega/2UQ$. Since variations in attenuation are typically much larger than variations in group velocity U, variations in α can be attributed to attenuation. Substituting eq. (1) into eq. (2) and separating the real and imaginary parts results in the two equations that are central to the analysis presented in this paper:

$$\frac{1}{c^2} = \nabla\tau\cdot\nabla\tau - \frac{\nabla^2(A/\beta)}{\omega^2(A/\beta)} \tag{3}$$

and

$$\frac{2\nabla\beta\cdot\nabla\tau}{\beta} - \frac{2\alpha}{c} = \frac{2\nabla A\cdot\nabla\tau}{A} + \nabla^2\tau, \tag{4}$$

where all dependencies on $\mathbf{r}$ have been dropped. With $\beta = 1$, eq. (3) provides the basis for determining variations in phase velocity via Helmholtz tomography (Lin & Ritzwoller 2011). Eq. (4) provides the basis for determining variations in attenuation from observations of surface wave amplitude and phase. The two terms on the right-hand side of eq. (4) contain the observables: variations in amplitude along the direction of wave propagation, and the Laplacian of the traveltime surface, which describes the focusing and defocusing effects. Following Lin *et al.* (2012), we refer to these terms as the 'apparent amplitude decay term' and 'focusing correction term', respectively, with the entire right-hand side as the 'corrected amplitude decay'. The left-hand side of eq. (4) contains the unknown quantities $\beta(\mathbf{r})$ and $\alpha(\mathbf{r})$. (We assume that $c(\mathbf{r})$ in eq. (4) is known from application of eq. (3) to the data, and that $\beta = 1$ in eq. (3) but not eq. (4).) The first term on the left-hand side is the 'amplification term', and the second term is the 'anelastic attenuation term'. It is clear from eq. (4) that the observables (i.e. the corrected amplitude decay) depend on both the local site amplification β and the attenuation coefficient α, and separating the relative contributions of these two factors is one of the primary challenges of imaging attenuation with the USArray data set. As described below, we consider three approaches for separately constraining β and α terms: the curve-fitting approach, the azimuthal-averaging approach, and independent constraints on local site amplification. The other significant challenge, discussed in Section 6, concerns the extent to which the Laplacian of the traveltime field can accurately account for focusing effects when actual traveltime measurements are used to compute that quantity.

Indeed, isolating the signal of attenuation in surface wave amplitude data is the primary challenge of all surface wave attenuation studies and is the main reason that attenuation tomography has historically lagged behind velocity tomography. In a general sense, a measured surface wave amplitude $A(\omega)$ can be considered to depend on four factors

$$A(\omega) = A_S(\omega)A_R(\omega)A_F(\omega)A_Q(\omega), \tag{5}$$

where A_S describes the effect of excitation at the earthquake source, A_R is the receiver term and describes the effect of local site amplification and the instrument response, A_F describes geometrical spreading and focusing/defocusing effects, and A_Q describes the decay due to attenuation along the propagation path (Dalton & Ekström 2006a,b). The receiver term (β), focusing effects ($\nabla^2\tau$), and attenuation (α) are all included in eq. (4). We note that values of β obtained from our analysis may reflect not only elastic structure in the crust and mantle beneath the station but also issues with the assumed instrument response (e.g. Ekström *et al.* 2006; Eddy & Ekström 2014). Although the effects of the earthquake source radiation pattern on amplitude are not considered in eq. (4), it is assumed that for a given event the azimuthal spread of stations is sufficiently narrow that variations in the source radiation pattern are small and can be neglected. We have examined this assumption by directly calculating and correcting for azimuthal variations in source amplitude using the Global CMT solution (e.g. Ekström *et al.* 2012; Dalton *et al.* 2013) for each event. We found that the effects on the retrieved attenuation maps are negligible, especially relative to the other sources of uncertainty.

3.2 Curve-fitting approach

In the high-frequency approximation, the amplitude Laplacian term in eq. (3) can be neglected, which reduces eq. (3) to

$$\hat{k} = c\nabla\tau, \tag{6}$$

where $\hat{k}$, the unit wave number vector, describes the direction of wave propagation. Defining the variable θ as the azimuth of propagation, eq. (6) can be written in Cartesian coordinates

$$\sin\theta\hat{x} + \cos\theta\hat{y} = c\left(\frac{\partial\tau}{\partial x}\hat{x} + \frac{\partial\tau}{\partial y}\hat{y}\right), \tag{7}$$

and it follows that

$$\tan\theta = \frac{\partial\tau/\partial x}{\partial\tau/\partial y}. \tag{8}$$

By substituting the high-frequency approximation, eq. (4) can be written as

$$\frac{\partial(\ln\beta)}{\partial x}\sin\theta + \frac{\partial(\ln\beta)}{\partial y}\cos\theta - \alpha = \frac{c}{2}\left(\frac{2\nabla A\cdot\nabla\tau}{A} + \nabla^2\tau\right). \tag{9}$$

The left-hand side of eq. (9) contains the three parameters that can be adjusted to fit the corrected amplitude decay: a coefficient multiplying the sine term, a coefficient multiplying the cosine term, and a static offset. The azimuth θ can be obtained from eq. (8), and then curve-fitting is used to estimate $\partial(\ln\beta)/\partial x$, $\partial(\ln\beta)/\partial y$, and α. Results obtained from applying this approach to USArray data in the western United States were described by Lin *et al.* (2012). As described in Section 5, this procedure is performed on each individual pixel, and the various earthquakes that contribute amplitude and traveltime information to that pixel define a range of corrected-amplitude-decay values that vary as a function of azimuth. This approach, which we refer to as the curve-fitting approach, yields constraints on lateral variations in both β and α. From the estimates of $\partial(\ln\beta)/\partial x$ and $\partial(\ln\beta)/\partial y$ we determine β based on a 2-D central finite-difference approximation in the Cartesian coordinate system:

$$\left.\frac{\partial(\ln\beta)}{\partial x}\right|_{x_0,y_0} = \frac{\ln\beta_{x_0-1,y_0} + \ln\beta_{x_0+1,y_0} - 2\ln\beta_{x_0,y_0}}{\Delta_{x_0-1,x_0} + \Delta_{x_0,x_0+1}}, \tag{10}$$

$$\left.\frac{\partial(\ln\beta)}{\partial y}\right|_{x_0,y_0} = \frac{\ln\beta_{x_0,y_0-1} + \ln\beta_{x_0,y_0+1} - 2\ln\beta_{x_0,y_0}}{\Delta_{y_0-1,y_0} + \Delta_{y_0,y_0+1}}, \tag{11}$$

where (x_0, y_0) is the central pixel, and Δ is the distance between nearby pixels in the x or y direction. Subscripts show the coordinates of four pixels surrounding the central pixel. We require that the sum of all $\ln\beta$ values in the study area is zero, which means that the site amplification values are not absolute but relative to the mean value of the site amplification in the study area.

3.3 Azimuthal-averaging approach

It was pointed out by Lin *et al.* (2012) that the attenuation coefficient α does not depend on azimuth (eq. 9). Thus, we can obtain an estimate of α by averaging the corrected amplitude decay values over azimuth. With this approach, referred to as the azimuthal-averaging approach, we do not obtain constraints on β.

3.4 Independent constraints on local site amplification

Eddy & Ekström (2014) constructed maps of local site amplification (β) using Rayleigh waves recorded by USArray stations. They calculated the ratio of surface wave amplitudes from an earthquake recorded at adjacent stations. If the effects of the source and propagation (e.g. focusing, attenuation) are highly similar at a pair of stations, the ratio should isolate effects associated with the local Earth structure at the receivers and problems in the instrument responses. The local site amplification at individual stations can then be obtained through least-squares inversion of the amplitude ratios. For our third approach we substitute the β values obtained by Eddy & Ekström (2014) into eq. (4) and solve for α. In Section 5.1, we also show results obtained when we apply the approach of Eddy & Ekström (2014) to our own amplitude data set.

4 PHASE-VELOCITY MAPS

For each event, surfaces of relative traveltime and amplitude are constructed using a minimum-curvature surface-fitting technique (Smith & Wessel 1990) applied to a $0.25^{\circ} \times 0.25^{\circ}$ grid and smoothed using a Gaussian filter with a radius of 100 km. Fig. 2 shows examples of the relative traveltime and amplitude surfaces for four events.

Eq. (3) is applied to the traveltime and amplitude surfaces in order to estimate phase-velocity variations for each event. The gradient of traveltime is calculated using a three-point central finite difference, and the Laplacian of amplitude is calculated using a five-point finite difference. Combining these quantities and taking the square root results in a map of variations in $1/c$ for each event. The individual (event-specific) $1/c$ maps are stacked by calculating the average $1/c$ value in each pixel. The stacking procedure occurs over two steps. In the first step, all individual $1/c$ values that contribute to a given pixel are included, yielding an initial estimate of phase velocity c_1 for that pixel. In the second step, outliers, identified as individual values for that pixel that fall outside of ± 5 per cent of $1/c_1$, are removed, and an updated value of phase velocity (c_2) for that pixel is calculated from the selected data set. Outlier selection typically removes about 20 per cent of the individual $1/c$ values in each pixel, and we have found that our results are not very sensitive to the value of this threshold. Fig. 3(a) shows the number of individual events that contribute to the final phase-velocity map in each pixel. The north–south-oriented stripes that are visible in the hit-count map reflect a combination of the non-uniform deployment duration of USArray stations, the non-uniform occurrence of the earthquakes that contributed to our data set, and a criterion that governs which pixels are included in the event-specific phase-velocity maps (i.e. prior to stacking). For a pixel to be included, there must be more than 10 stations located within 150 km of that pixel and, to ensure a distribution of azimuths, there must be at least one of these nearby stations in each azimuthal quadrant. This criterion is used to reduce the possible bias introduced by the smoothing procedure near the edge of each event-specific map. Our data processing for site amplification and attenuation is then based on the event-specific maps determined with this criterion.

Fig. 4 shows the stacked phase-velocity maps at 25, 40, 50 and 60 s. The east–west separation in velocity along the vicinity of Rocky Mountain front is clearly observed, as are low velocities associated with the Yellowstone hotspot, Snake River Plain, the Basin and Range, and the Rio Grande Rift at longer periods. At 25 s anomalously low velocities are associated with the deep crustal roots beneath the Rocky Mountains and the Mid-Continent Rift. Correlation coefficient with the phase-velocity maps of Jin & Gaherty (2015), which were constructed using the same data set, are >0.94 for periods 25–80 s and 0.88 at 100 s. Correlations with the phase-velocity maps of Ekström (2014), which were constructed from ambient-noise data, are larger than 0.94 at 25, 32 and 40 s. Gaussian smoothing over a 400-km radius was applied to our phase-velocity maps for these comparisons.

Fig. 5 provides two estimates of uncertainty in the phase-velocity maps. Uncertainties summarized in Figs 5(a) and (c) are determined from the distribution of the individual phase-velocity values that contribute to the average value in each pixel (i.e. eq. (7) in Lin *et al.* 2009). The uncertainty is typically <10 m s^{-1}, consistent with other published estimates (Lin & Ritzwoller 2011), and there is little geographic variation in the uncertainty estimates across the array, perhaps due in part to the process of outlier removal described above. The uncertainty summarized in Figs 5(b) and (d) results from a comparison of the left-hand and right-hand sides of eq. (3):

$$M_j = \frac{1}{N}\sum_{i=1}^{N}\left[\frac{1}{c_j^2} - \left((\nabla\tau)_{ij}\cdot(\nabla\tau)_{ij} - \frac{(\nabla^2 A)_{ij}}{\omega^2 A_{ij}}\right)\right]^2. \tag{12}$$

The uncertainty in pixel j is estimated from the sum over the N individual events that contribute to the phase velocity in that pixel, c_j, of the squared difference between the observations (surfaces) of traveltime and amplitude for the ith event in the jth pixel and the stacked phase-velocity maps. The inverse of the fourth root of M_j is plotted in Figs 5(b) and (d), yielding a quantity with units of m s^{-1}. We attribute the larger uncertainty in the west to imperfect estimates of the Laplacian of the amplitude field (eq. 3), which will vary more significantly with wave propagation direction in the strongly heterogeneous west than in the more homogeneous east and may be limited by the 70-km spacing of USArray (Lin & Ritzwoller 2011).

5 RAYLEIGH WAVE ATTENUATION AND SITE-AMPLIFICATION MAPS

5.1 Curve-fitting approach

Fig. 6 shows the corrected amplitude decay values in eight pixels. In all eight cases a 360° periodicity is apparent; the individual values exhibit some scatter about this trend. In Figs 7(a)–(c) and 8 we show maps of β and attenuation obtained for 50-s Rayleigh waves using the curve-fitting approach applied to three subsets of the data: (i) all corrected amplitude decay values; (ii) corrected amplitude decay values that have been selected using a criterion on arrival

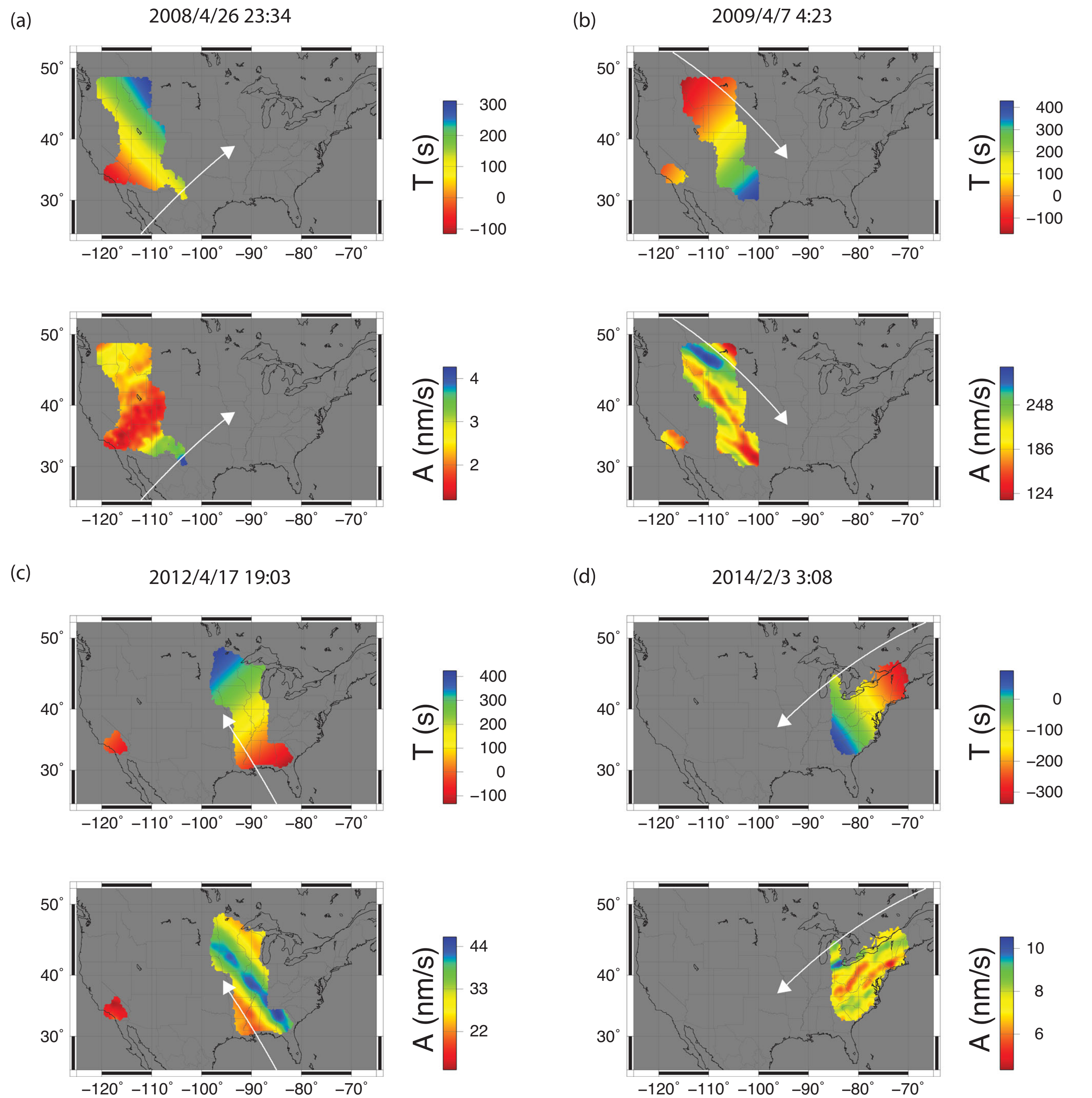

Figure 2. Single-station traveltimes and amplitudes measured for 50-s Rayleigh waves from (a) a M_w 5.9 event in the Auckland Islands, New Zealand; (b) a M_w 6.9 event in the Kuril Islands; (c) a M_w 6.2 event near the South Sandwich Islands and (d) a M_w 6.0 event in Greece. These figures show traveltime and amplitude surfaces constructed from the measurements as described in Section 4.

angle and (iii) median values of the selected corrected amplitude decay values, calculated in a sliding 20° azimuthal window. For each event and pixel, arrival angle is estimated from eq. (8). Arrival angles in nearby pixels (pixels within radius = 150 km) are compared. If the arrival angle in the central pixel varies by more than 2° from the average of the arrival angle in the nearby pixels, the corrected amplitude decay value from that event and pixel is eliminated. This criterion is designed to identify paths that have been strongly bent, which would likely be accompanied by strongly distorted amplitudes. The corrected amplitude decay values that remain after this selection process are indicated by blue circles in Fig. 6, and their median values, calculated in sliding 20° azimuthal bins, are shown by the red circles. Fig. 3(b) shows the number of events that contribute data to each pixel after selecting arrival angles.

Fig. 8 shows examples of attenuation maps obtained with no smoothing applied and with Gaussian smoothing applied using a 400-km radius. The smoothed maps are shown to help emphasize the long-wavelength structure; features near the perimeter of these maps have large uncertainties. Comparison of these six attenuation maps helps to highlight the features in the maps that are

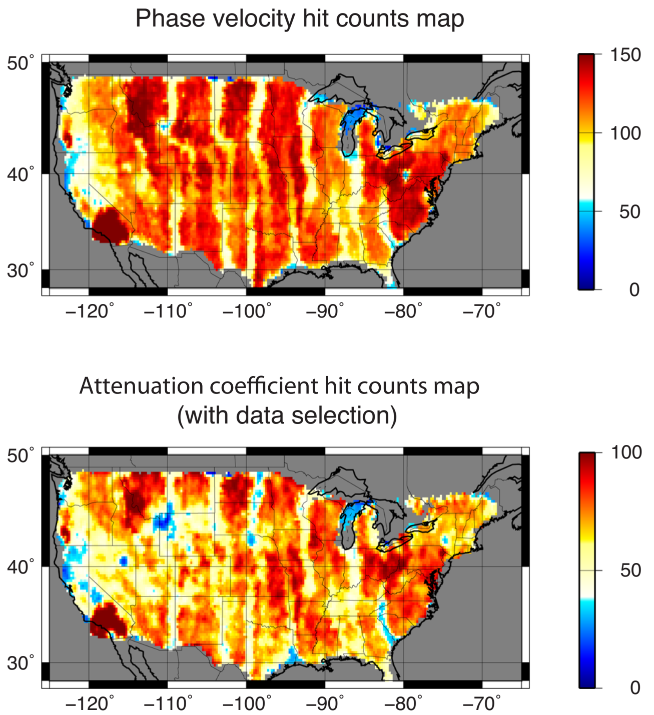

Figure 3. (a) Number of events that contribute to each $0.25^\circ \times 0.25^\circ$ pixel for the 50-s Rayleigh wave phase-velocity maps. (b) Number of events that contribute to each $0.25^\circ \times 0.25^\circ$ pixel for the 50-s Rayleigh wave attenuation maps that were obtained using the curve-fitting approach applied to selected corrected amplitude decay based on azimuth.

sensitive to decisions about which data are included in the curve-fitting approach. All maps resolve a general west-to-east decrease in attenuation across the continent, which has been observed by previous global surface wave (Dalton *et al.* 2008) and regional body-wave (Lawrence *et al.* 2006; Hwang *et al.* 2009) studies. A corresponding west-to-east velocity increase can be found in the 50-s phase-velocity map (Fig. 4). It is apparent from Fig. 8(top) that when all values of corrected-amplitude decay are used as input to the curve-fitting approach, the enhanced scatter of these values (Fig. 6) results in a noisier image of attenuation, although we note that the β values are not significantly impacted (Fig. 7a). Applying some selection criteria to these values results in an image that shows a more distinct west-to-east transition, and hints at a return to higher attenuation beneath the northeastern United States. There is little difference between the attenuation maps determined from the selected and median values of corrected amplitude decay (Fig. 8 middle and bottom). Both sets of maps also show that the overall high attenuation in the west is interrupted at several places by extremely low attenuation; indeed, at some locations the $1/Q$ values obtained from the curve-fitting approach are negative. Since negative attenuation is physically impossible and since most of the low-attenuation anomalies in the west do not have a corresponding high-velocity feature in the 50-s phase-velocity map and in fact correspond to zones of very low wave speed, we suspect that these anomalies may be artefacts that arise from an imperfect treatment of focusing effects. We investigate this issue in Section 6.

Figs 7(a)–(c) show good agreement between the three sets of β maps; correlation coefficient R, calculated for 1990 station locations, is 0.68 between Figs 7(a) and (b), 0.69 between Figs 7(a) and (c), and 0.99 for Figs 7(b) and (c). Of these three maps, we have the least confidence in the β map in Fig. 7(a), which was determined using all values of corrected amplitude decay, an approach that may yield some anomalous values in pixels with uneven azimuthal coverage. The correlation coefficient between the map in Fig. 7(c) and the map published by Eddy & Ekström (2014) (Fig. 7d) is 0.57. We determine an additional β map by applying the approach of Eddy & Ekström (2014) to our data set (Fig. 7e). At the whole-continent scale, the correlation coefficient between the two maps (Figs 7d and e) determined using the approach of Eddy & Ekström (2014) is 0.56. However, when we examine the correlation in restricted longitude bands, agreement is much better. For example, $R = 0.77$ for the 163 stations with longitudes in the range –115°E to –110°E and $R = 0.87$ for the 186 stations with longitudes in the range –95°E to –90°E. For all 5°-wide longitude bands west of 85°W the correlation coefficient between the two sets of β values is >0.7, much higher than the whole-continent value would indicate. The ratio of our β values to the β values of Eddy & Ekström (2014) varies across the array as a function of longitude; thus, when all values are lumped together for the whole-continent comparison the longitude-dependent trends are lost. We suspect that the differences between the two sets of maps may reflect differences in the azimuthal coverage of the two amplitude data sets, as we have found that there are differences in the β maps obtained when we restrict the azimuthal coverage of our data set. Finally, we note that the β maps obtained with the curve-fitting approach are not identical to the maps obtained with the amplitude-ratio approach. The level of agreement at the whole-continent scale ($R = 0.57$) is similar to that reported by Eddy & Ekström (2014) for the comparison in the western United States of their results and those of Lin *et al.* (2012) ($R = 0.67$). It is also similar to a comparison performed by Eddy & Ekström (2014) of their results with β values predicted using 3-D crust and mantle seismic models ($R \approx 0.45$ at 50 s). One explanation for the differences may be that the assumption on which the amplitude-ratio approach is based—that dividing the amplitudes cancels out the effects of propagation and the source—is not perfectly met. This issue will be especially problematic when the distribution of earthquakes available to a pair of stations provides highly non-uniform azimuthal coverage, which could result in, for example, unmodelled focusing effects being absorbed by the β values. In Section 5.3 the implications of the different β maps on the attenuation structure are explored.

5.2 Azimuthal-averaging approach

Fig. 9 shows 50-s attenuation maps obtained by applying the azimuthal-averaging approach to (i) all corrected amplitude decay values and (ii) corrected amplitude decay values that have been selected using the criterion on arrival angle. Maps are shown with no smoothing applied and with Gaussian smoothing applied over a 400-km radius. We follow Lin *et al.* (2012) and compute a weighted average of the individual corrected amplitude decay values to avoid bias from uneven source coverage. The number of measurements in each 25° azimuthal bin is calculated, and the weight applied to each measurement is the reciprocal of the number of measurements in the associated bin.

The maps are generally similar to those in Fig. 8. The high degree of similarity is not surprising, considering that the curve-fitting and azimuthal-averaging approaches are essentially equivalent in cells where the azimuthal coverage is good. When all values of corrected amplitude decay are included, the result is generally higher attenuation throughout the study region than when only the selected values are considered. The west-to-east attenuation decrease is

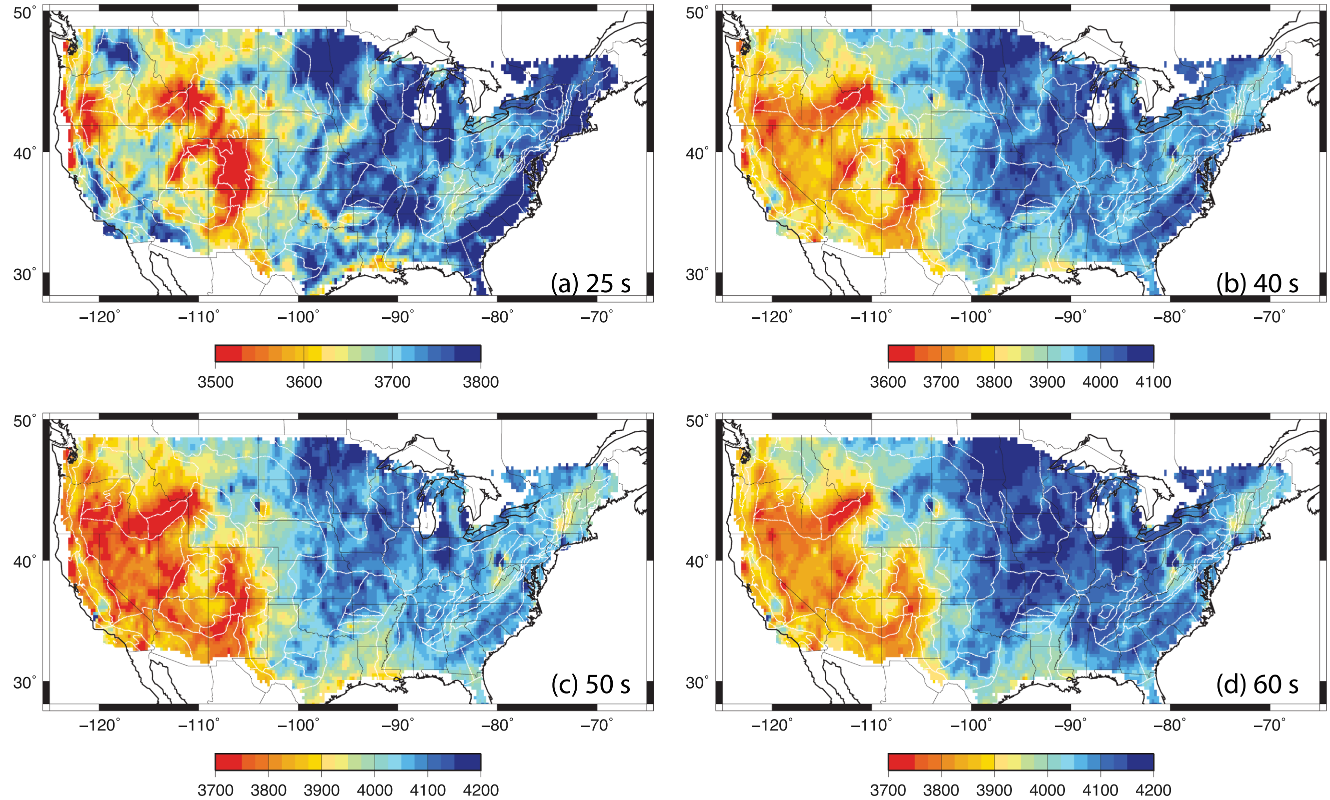

Figure 4. Rayleigh wave phase-velocity (in m s^{-1}) maps at 25, 40, 50 and 60 s. Thin white lines are tectonic boundaries.

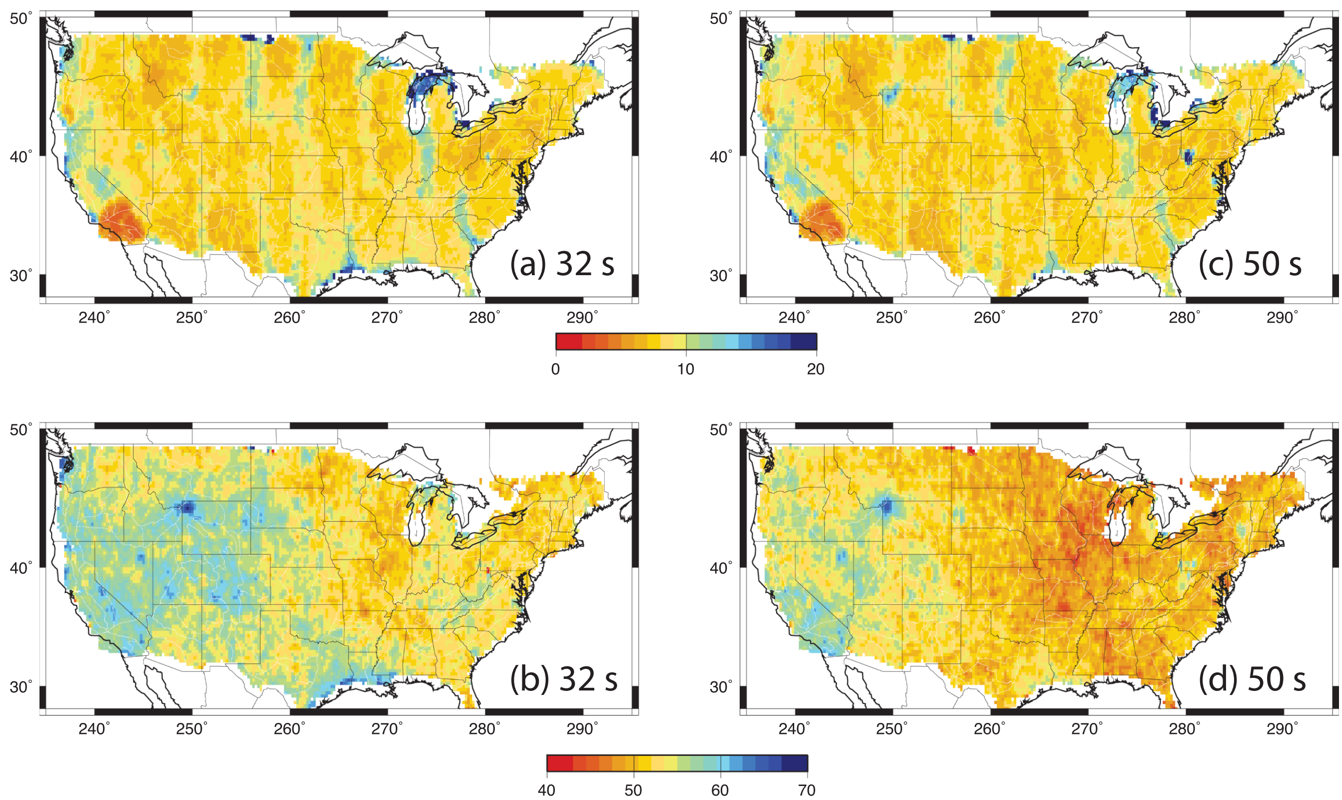

Figure 5. Uncertainty in phase-velocity maps. Top panel: uncertainty determined from the width of the distribution of individual phase-velocity values that contribute to each pixel. Bottom panel: uncertainty determined from eq. (12); inverse of the 4th root of uncertainty is plotted. Left-hand column: 32 s. Right-hand column: 50 s. Units are m s^{-1}.

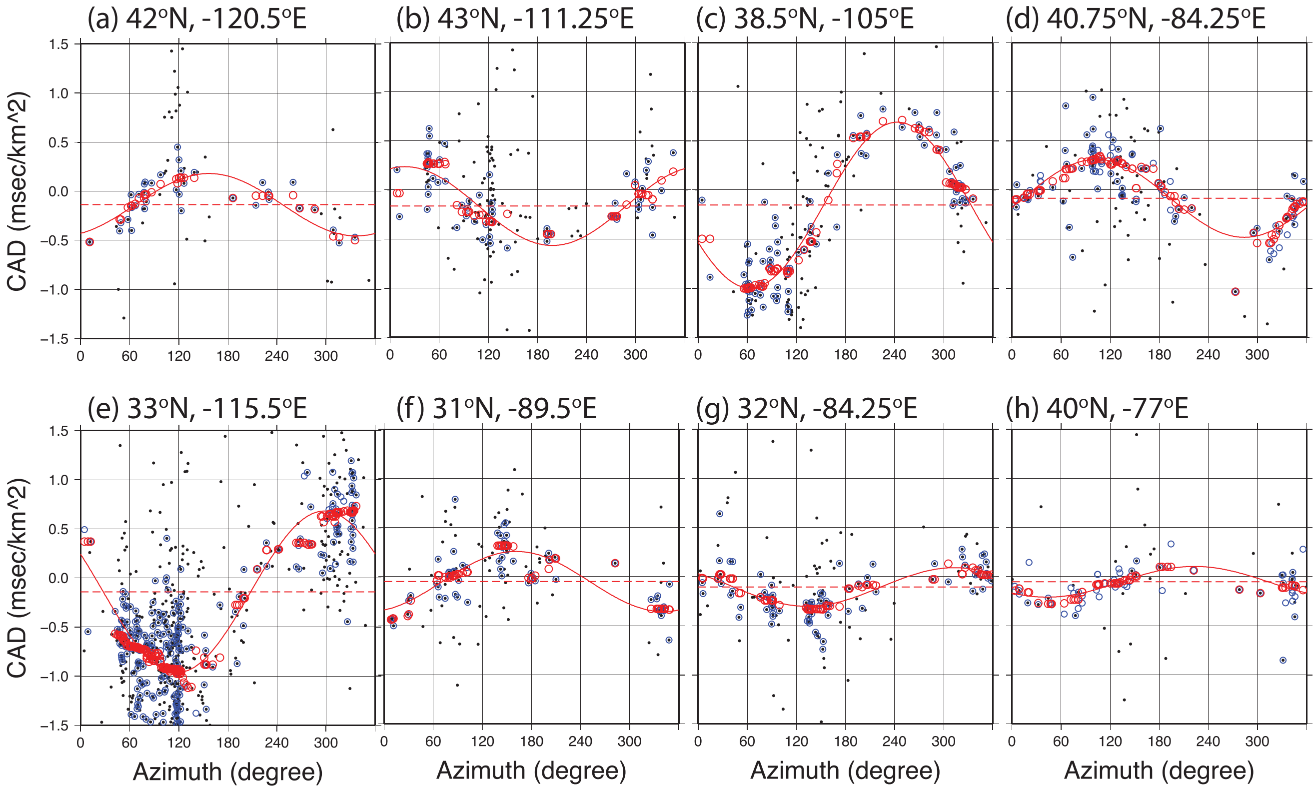

Figure 6. Examples from 8 pixels of the curve-fitting approach applied to values of corrected amplitude decay. Values from all contributing events are indicated with small black dots. Values selected based on an arrival-angle criterion are indicated with blue circles. Red circles show median of selected values in a sliding 20° azimuthal window. Solid red line is the best curve fit to the median values; dashed red line indicates the value of $-2\alpha/c$ obtained with the curve-fitting approach.

visible in all maps, as is the slightly higher attenuation in the northeast. As we found with the curve-fitting approach, several zones of anomalously low attenuation are seen in the western United States and may originate from inadequate correction for focusing effects.

5.3 Independently determined amplification factors

Fig. 7(d) shows the 50-s β values determined by Eddy & Ekström (2014), and Fig. 7(e) shows the β values obtained by applying the approach of Eddy & Ekström (2014) to our amplitude data set. The spatial derivatives of these β maps can be readily calculated, which allows α values to be estimated from the corrected amplitude decay for each pixel and each event (eq. 4). The individual α maps for each event are then stacked to obtain a master α map, from which Rayleigh wave attenuation can be determined by

$$\alpha = \sum_{i=1}^{N}\left[-\frac{c_i \nabla (A_i/\beta)\cdot \nabla \tau_i}{A_i/\beta} - \frac{c_i}{2}\nabla^2 \tau_i\right], \tag{13}$$

where the summation is over all available events for a given pixel location in the study area. Fig. 10 shows 50-s attenuation maps calculated using the two sets of independently determined local site amplification factors, with and without Gaussian smoothing. Note that the attenuation values in the far northeastern United States are characterized by high uncertainties when the β map of Eddy & Ekström (2014) is used since β values were not determined for those USArray stations in that study (Fig. 7d). The maps in Fig. 10 contain high attenuation in the west, low attenuation in the central and eastern United States, and slightly elevated attenuation along the eastern seaboard. Both sets of maps show a band of low attenuation oriented north–south and centred near −105°E (255°E), which is present but less prominent in the attenuation maps of Figs 8 and 9. Correlation between the two sets of values obtained using independently determined β values is 0.65 for the unsmoothed maps (Figs 10a and c) and 0.69 for the smoothed maps (Figs 10b and d). Some of the differences between the two sets of maps appear to be related to differences between the corresponding β maps (Figs 7d and e). For example, the overall larger values of β in the western United States obtained by Eddy & Ekström (2014) are balanced by overall larger values of attenuation; in other words, in the western United States the maps show higher amplification and higher attenuation for Eddy & Ekström (2014) and lower amplification and lower attenuation when the amplitude-ratio approach is applied to our data set.

The attenuation values obtained using the three different approaches exhibit the same large-scale features. For example, the correlation coefficient, calculated using 9860 pixels, between the unsmoothed curve-fitting and azimuthal-averaging attenuation maps (i.e. Figs 8e and 9c) is 0.66; this value increases to 0.69 when the smoothed versions of those maps are compared (Figs 8f and 9d). Agreement between the unsmoothed attenuation maps obtained using curve-fitting (Fig. 8e) and independently determined β values is weak—0.19 and 0.24 for Figs 10(a) and (c), respectively; it improves considerably for the smoothed versions of these attenuation maps, with correlation coefficients of 0.43 and 0.49, respectively. We note that these results are also obtained when the maps obtained using azimuthal averaging are compared to the maps obtained

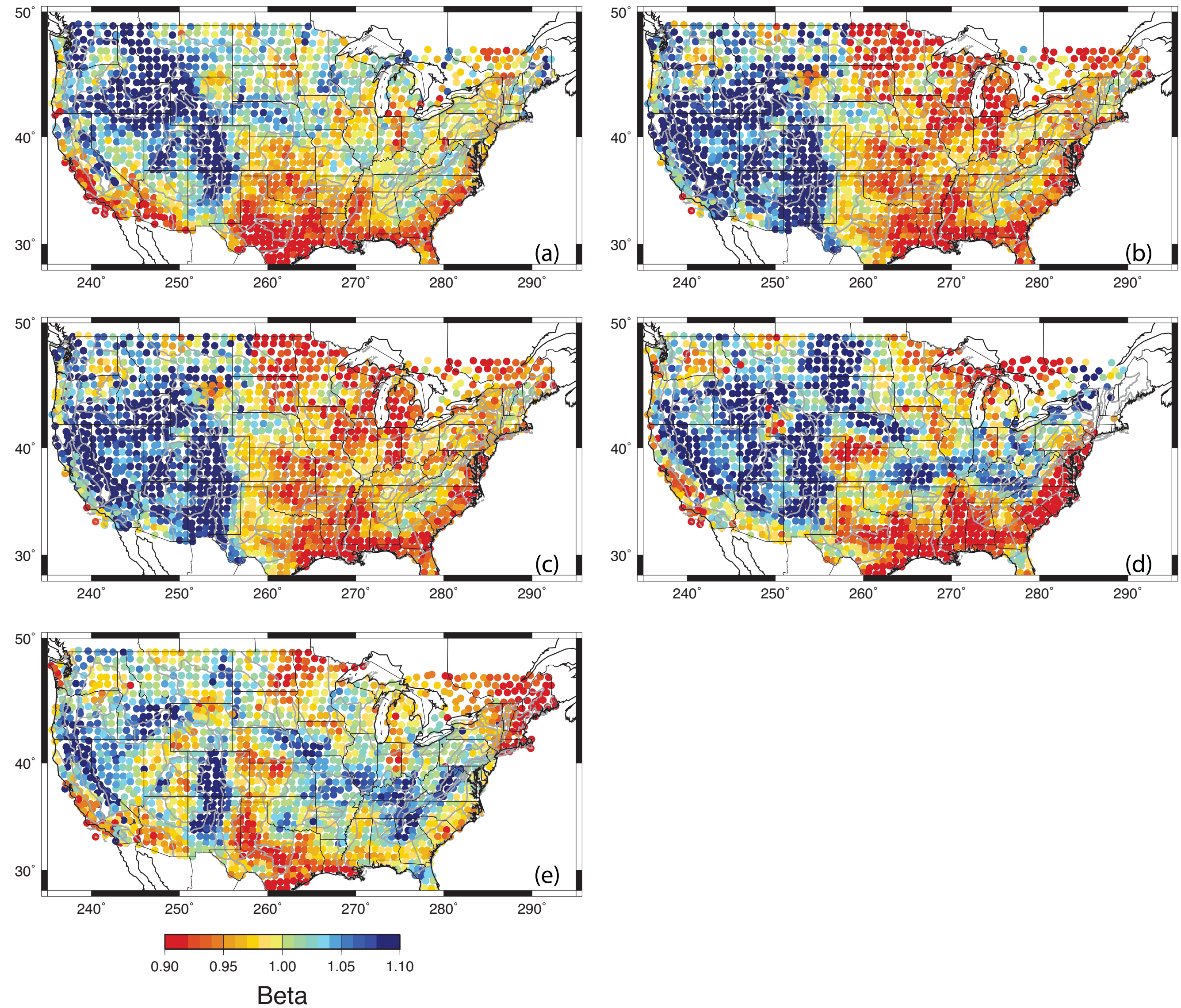

Figure 7. Maps of local site amplification (β) for 50-s Rayleigh waves. (a) Determined from curve-fitting approach applied to all values of corrected amplitude decay. (b) Determined from curve-fitting approach applied to selected values of corrected amplitude decay (see text). (c) Determined from curve-fitting approach applied to median values of corrected amplitude decay. (d) Values determined by Eddy & Ekström (2014) using ratios of amplitudes at nearby stations. (e) Values determined by applying the approach of Eddy & Ekström (2014) to our amplitude data set. In (a)–(c), the $0.25^\circ \times 0.25^\circ$ site amplification maps have been sampled at the locations of 1990 seismic stations.

using independently determined β values, as is expected given the similarity between the curve-fitting and azimuthal-averaging attenuation maps.

The most prominent difference between the attenuation maps obtained using curve-fitting/azimuthal-averaging and using independently determined β values is centred near 260°E/37°N, an area characterized by low attenuation in the former and high attenuation in the latter. The β values of this area also differ, with low amplification for the curve-fitting results (Fig. 7c) and higher amplification for the independently determined factors (Figs 7d and e). The sense of these differences is consistent with a trade-off between β and attenuation: low β and low attenuation for curve-fitting versus high β and high attenuation for independently determined amplification factors. Finally, we note that there is a practical difference in the way that the attenuation maps obtained with the curve-fitting/azimuthal-averaging approach and with independently determined β values are computed. In the latter case, the attenuation maps result from simply stacking all individual (event-specific) attenuation maps without any attempt to account for non-uniform azimuthal coverage; in the former case the curve-fitting/azimuthal-averaging approach accounts for dependence on azimuth. This difference in approach may contribute to differences between the maps in Figs 8 and 10.

Since the corrected amplitude decay values from which these attenuation maps are determined are sensitive to both attenuation and local site amplification, we prefer approaches that treat attenuation and local site amplification simultaneously rather than separately. Thus we focus on attenuation values obtained using the curve-fitting approach and the azimuthal-averaging approach in the remainder of this paper.

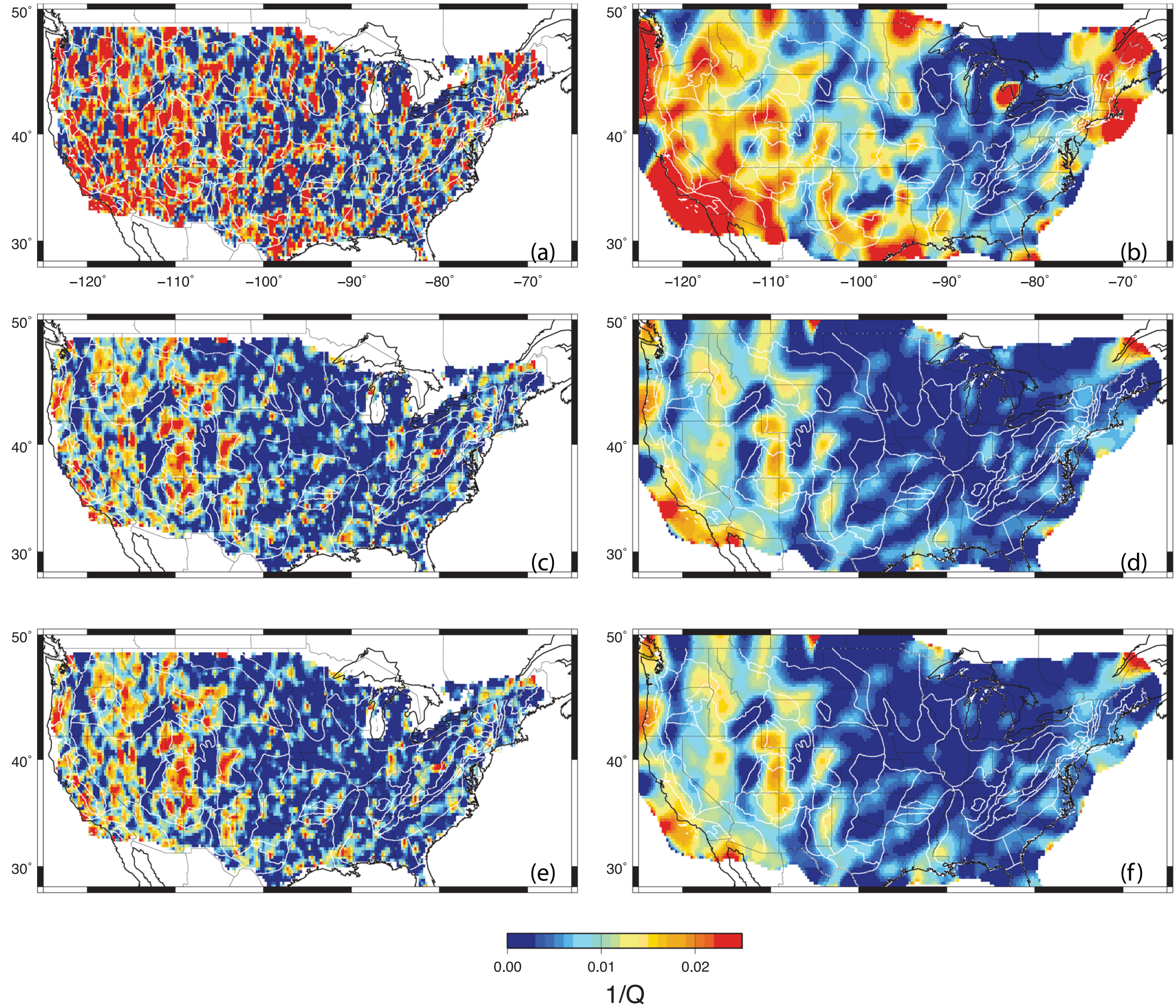

Figure 8. Maps of 50-s Rayleigh wave attenuation determined from curve-fitting approach. Top panel: determined from curve-fitting approach applied to all values of corrected amplitude decay. Middle panel: determined from curve-fitting approach applied to selected values of corrected amplitude decay. Bottom panel: determined from curve-fitting approach applied to median values of corrected amplitude decay. Values in left-hand column have not been smoothed; values in right-hand column have been smoothed using Gaussian smoothing with a 400-km radius.

6 TREATMENT OF FOCUSING EFFECTS

It is well established that focusing and defocusing effects due to propagation through elastic heterogeneity can have a significant impact on surface wave amplitudes. Dalton & Ekström (2006b) showed that global phase-velocity maps can be successfully retrieved from amplitude measurements alone. Selby & Woodhouse (2000) and Dalton & Ekström (2006a) have shown how unmodelled focusing effects on Rayleigh wave amplitudes can be mapped into attenuation anomalies on a global scale. Joint inversion of phase and amplitude measurements for shear-velocity models has been implemented in several studies (Yang & Forsyth 2006; Yang *et al.* 2007; Dalton *et al.* 2008). In recent years surface wave amplitudes have been utilized to correct for the bias between apparent phase velocity and structural phase velocity (eq. 3) in array-based studies (Lin & Ritzwoller 2011; Jin & Gaherty 2015).

In order to constrain anelastic attenuation with surface wave amplitudes, these focusing effects must first be removed from the amplitude data. With our approach this removal occurs through the Laplacian of the traveltime field in eq. (4). As discussed by Lin & Ritzwoller (2011) and Lin *et al.* (2012), while the Laplacian of the traveltime field can be theoretically used to correct for focusing effects, in practice its resolving power is limited by the 70-km station spacing of USArray. It is thus likely that the Laplacian of the traveltime field, and therefore the focusing correction, is underestimated. We expect that this underestimation will be most pronounced in regions containing strong local variations in velocity. For phase-velocity studies, the Laplacian of the amplitude field is a second-order term; it provides a meaningful correction to the apparent phase velocities determined from the gradient of the traveltime field (eq. 3), but the first-order features in the structural phase-velocity maps are also visible in the apparent phase-velocity maps (e.g. Lin

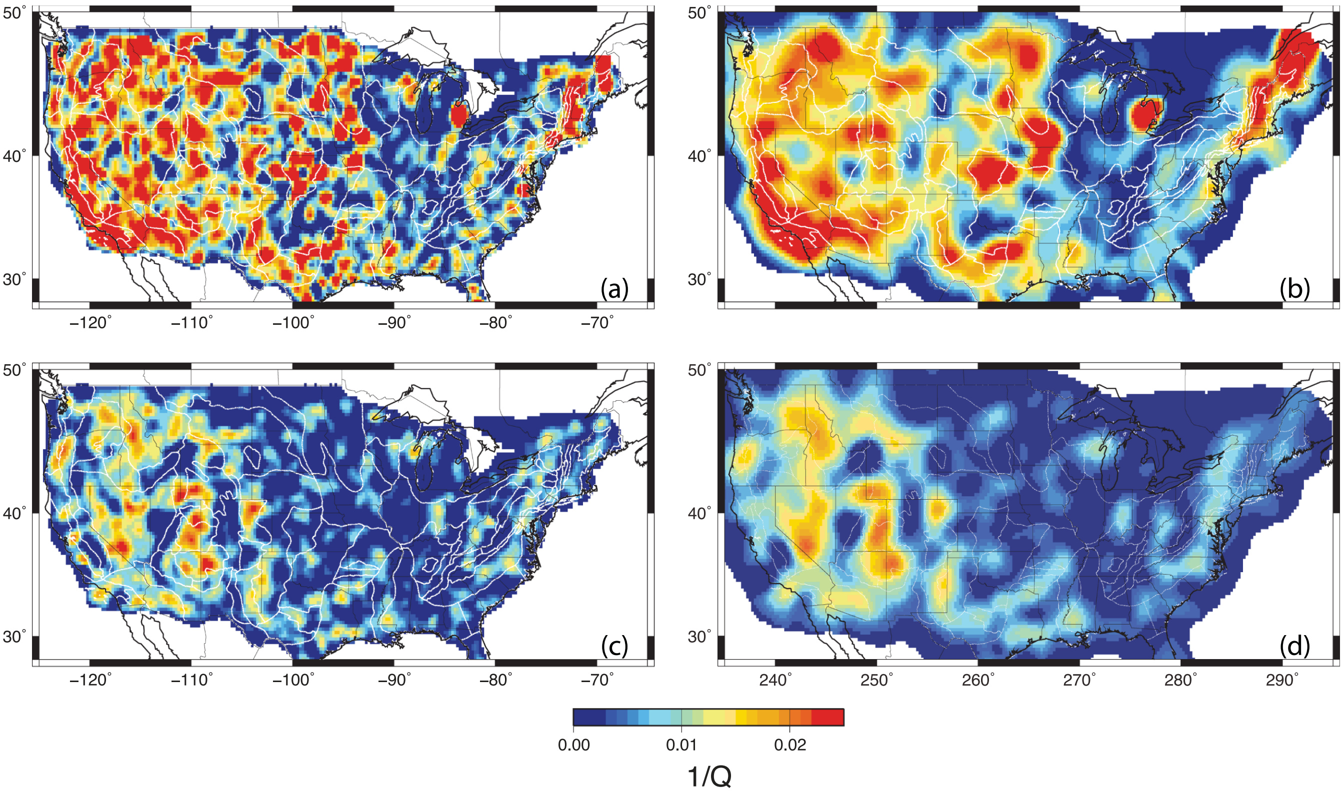

Figure 9. Maps of 50-s Rayleigh wave attenuation determined using azimuthal-averaging approach. Top panel: determined from azimuthal-averaging approach applied to all values of corrected amplitude decay. Bottom panel: determined from azimuthal-averaging approach applied to selected values of corrected amplitude decay. Values in left-hand column have not been smoothed; values in right-hand column have been smoothed using Gaussian smoothing with a 400-km radius.

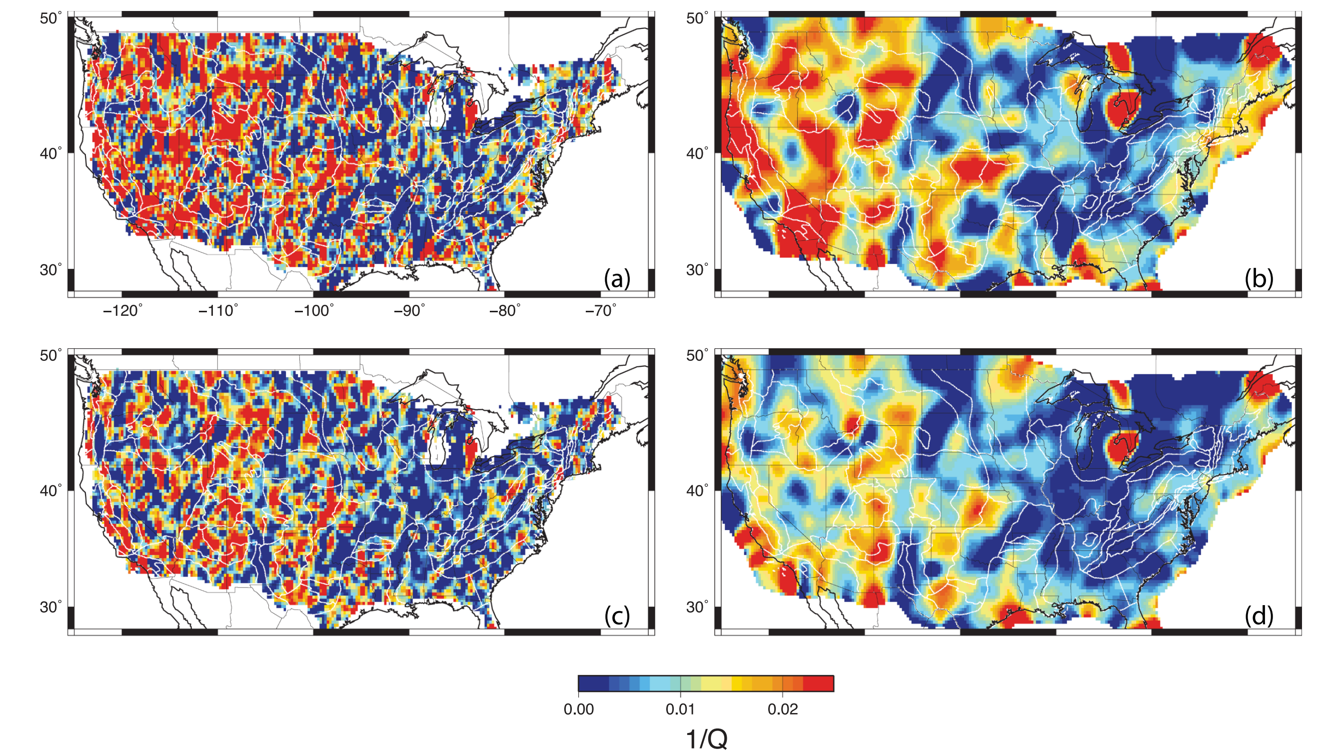

Figure 10. Maps of 50-s Rayleigh wave attenuation determined using independently constrained maps of local site amplification. Top panel: the site-amplification maps were determined by Eddy & Ekström (2014). Bottom panel: the site-amplification maps were determined by applying the approach of Eddy & Ekström (2014) to our data set. Values in left-hand column have not been smoothed; values in right-hand column have been smoothed using Gaussian smoothing with a 400-km radius.

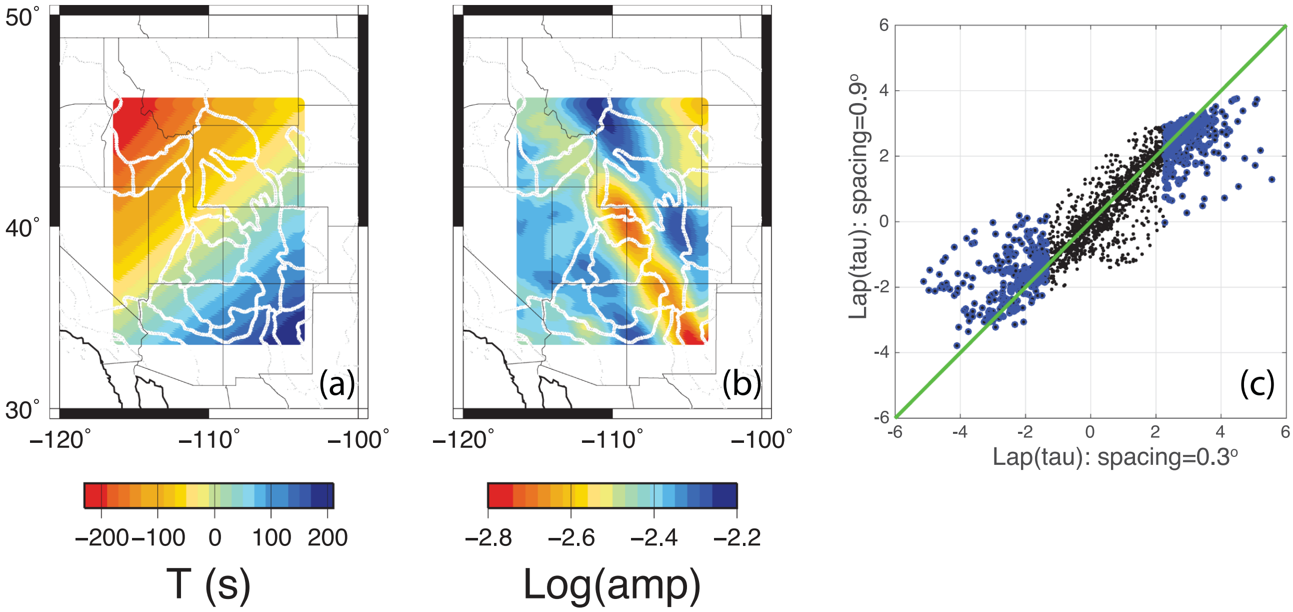

Figure 11. (a) Traveltimes of 50-s fundamental-mode Rayleigh waves determined from synthetic waveforms generated using a finite-difference method with a 3-D velocity model and an explosive source located to the northwest. Measurements are made at stations evenly spaced by 0.1°. (b) As in (a) but the amplitudes measured from the synthetic waveforms. (c) Comparison of the Laplacian of the synthetic traveltime field made using a station spacing of 0.3° and 0.9°. Black circles show the Laplacian calculated for 1876 pixels; blue circles highlight the comparison for the 643 pixels in which the Laplacian calculated with 0.3° spacing falls outside one standard deviation of the mean. The 1:1 line is shown in green.

& Ritzwoller 2011). This is not the case for the attenuation maps. The contribution of focusing to the amplitudes may be as large as (or larger than) the contribution of attenuation. An inadequate correction for focusing effects may therefore result in biased attenuation maps. Propagation through a low-velocity channel focuses wave energy and enhances surface wave amplitudes. Such high amplitudes can map into anomalously low attenuation if focusing effects are not properly accounted for. Propagation through a high-velocity channel defocuses wave energy, diminishing wave amplitudes and mapping into anomalously high attenuation if focusing effects are not properly accounted for.

6.1 Wavefield simulation using a 3-D finite-difference method

To explore whether focusing and defocusing effects might be underestimated by the observed traveltime field, we simulate wave propagation using a collocated-grid finite-difference method in spherical coordinates (Zhang *et al.* 2012). The computations take place on a Linux cluster containing 1160 CPU cores and 180 TB disk space at the University of Rhode Island. This algorithm has been shown to provide an excellent fit to surface waves (Zhang *et al.* 2012). Gao & Shen (2015) used this method to validate 3-D velocity models for United States by simulating regional Rayleigh waves and empirical Green's functions extracted from ambient noise in the period range 15–75 s.

The simulations described here utilize a 3-D velocity model with no attenuation, in which the regional shear velocity (V_S) model for the western United States described by Shen *et al.* (2013) is imbedded within CUB2.0, a global anisotropic shear-wave velocity model of Shapiro & Ritzwoller (2002). CUB2.0 is parameterized in elements with dimensions of $2^\circ \times 2^\circ$ laterally and 4 km radially from the surface to 396-km depth. The regional model of Shen *et al.* (2013), which covers the United States west of 100°W, has a laterally uniform grid size of $0.25^\circ \times 0.25^\circ$ and non-uniform grid spacing in vertical direction down to 200-km depth. Both models are sampled onto the same parameterization; smoothing and interpolation occurs at the edges of the regional model to allow a smooth transition into the global background model. The combined model used for the finite-difference simulations has a lateral grid spacing of 0.05° and a vertical grid spacing that increases with depth from ~1.8 km near the surface to ~7 km at 400 km, which is the maximum depth of the model. This model is appropriate for Rayleigh waves of periods longer than ~25 s. Compressional-wave speed (V_P) is estimated from V_S using $V_P/V_S = 1.74$ for the crust (Brocher 2005) and the V_P/V_S ratio from AK135 (Kennett *et al.* 1995) for the mantle. Density is estimated by adopting the empirical relationship between V_P and density (Christensen & Mooney 1995).

The objective of the wavefield simulations is to provide a complete theoretical description of the effect on wave propagation of complicated elastic heterogeneity in the crust and upper mantle of the western United States, including complexities like wave front healing, multipathing, multiple scattering, and focusing/defocusing. Although the combined 3-D velocity model may not fully represent realistic Earth structures, that aspect of the model is not important for the tests described below, since we do not compare the synthetic waveforms to observations made on the real Earth.

Synthetic seismograms are generated for an explosive source located at 10-km depth and 30° to the northwest of the centre of the array; the source–time function is a Bell-integral function with duration of 5 s. Ellipticity, anisotropy, surface topography, and attenuation are not considered in the simulation. The wavefield is sampled at 'stations' located at grid nodes separated by 0.1°, and the ASWMS algorithm is utilized to measure the amplitude and relative traveltime of the fundamental-mode Rayleigh wave at each station. Figs 11(a) and (b) show the synthetic traveltime and amplitude measurements for 50-s Rayleigh waves.

6.2 Dependence of Laplacian on station spacing

The synthetic data set is used to compute the Laplacian, using a five-point finite difference, for different values of the station spacing. Fig. 11(c) shows a comparison for 1876 pixels of Laplacian values calculated using 0.3° station spacing and 0.9° station spacing. For 52 per cent of these pixels the ratio of Laplacian values calculated with the smaller and larger station spacing is >1, indicating a larger magnitude of Laplacian for the smaller station spacing. A more useful comparison, however, is how station spacing affects the Laplacian computed in pixels for which the magnitude of the Laplacian is large. Fig. 11(c) highlights in blue the 643 pixels for which the Laplacian calculated with 0.3° spacing falls outside one standard deviation of the mean. For 79 per cent of these pixels, the magnitude of the Laplacian calculated with 0.3° spacing is larger than with the 0.9° spacing. The median value of the ratios for these 509 pixels is 1.23, indicating that the magnitude of the Laplacian is on average 23 per cent larger when calculated with the smaller station spacing.

These calculations show that the magnitude of the Laplacian depends on station spacing and is likely to be underestimated when a coarser station spacing is used, especially in pixels where the magnitude of the Laplacian is large. Changes in the value of the Laplacian would directly impact the values of the corrected amplitude decay (Fig. 6) as well as the attenuation and local amplification parameters estimated from those values. A valuable next step would be to determine attenuation and local amplification maps for our synthetic data set, which will be a high priority for future work.

6.3 Determining regionally averaged attenuation maps

A conclusion drawn from Fig. 11(c) is that computing the focusing correction with a synthetic traveltime field could be more accurate than computing it with the actual traveltime field; the fact that USArray has yielded high-resolution seismic-velocity images for North America makes this approach even more compelling. To do this accurately would require, for example, 3-D finite-difference or spectral-element computations for each of the 882 events in our data set and is beyond the scope of this study. For this study we adopt the following approach. We compute the Laplacian of the phase-velocity map and identify pixels with large absolute values of the Laplacian. We assume that the attenuation values in these pixels may be biased and remove them from the original maps. We apply one additional adjustment to the attenuation values that remain after this selection process; any attenuation values $<1/600$ are fixed to a value of 1/600. (We also require any attenuation values $>1/30$ to be fixed to a value of 1/30, but in practice there are very few attenuation values that meet this criterion.) The choice of lower bound (1/600) reflects the fact that Rayleigh wave amplitudes cannot resolve small differences in low-attenuation values, and the choice of upper bound (1/30) reflects the high-attenuation values obtained in a variety of regional and global attenuation studies. The choice of bounds on Rayleigh wave attenuation is guided by results from previous regional and global studies (e.g. Yang *et al.* 2007; Dalton *et al.* 2008; Yang & Forsyth 2008; Lin *et al.* 2012). Since the resulting maps are missing attenuation values in certain areas, we then perform regional averaging of the available attenuation values within a prescribed radius. In constructing these regionally averaged maps we have made our best effort to account for focusing and site-amplification effects and to eliminate individual attenuation values in which we have little confidence. However, we also recognize that our attempt to account for unmodelled focusing effects is only approximate and that the regional averaging smooths local variations, especially in areas from which we removed the attenuation values, and likely underestimates the true magnitude of attenuation variations across the continent.

Fig. 12(b) shows the Laplacian of the 50-s phase-velocity map. When compared to the attenuation values obtained using the azimuthal-averaging approach (Fig. 12a), there is a clear correspondence between some of the extremely low attenuation values in the western United States and areas where the value of the Laplacian is large and positive. There is also some correspondence between values of the Laplacian that are large and negative and extremely high attenuation values in the west. We note, however, that while the Laplacian does contain more strongly heterogeneous values in the west than in the east, there is not a significant contrast in the average value of the Laplacian in the west versus the east, lending confidence to our interpretation that the west-to-east decrease in attenuation that is present in all of our attenuation maps (Figs 8–10) reflects actual changes in the Earth's anelastic properties and is not somehow introduced by the treatment of focusing effects. Fig. 12(c) shows the individual attenuation values after removing pixels where the absolute value of the Laplacian of phase velocity is $>5 \times 10^{-9}$ and applying the lower and upper bounds 1/600 and 1/30, respectively. The threshold on the Laplacian is determined through trial and error and is chosen based on its ability to identify pixels characterized by clearly anomalous attenuation in the western United States. Increasing this value removes fewer pixels and reducing it removes additional pixels. Fig. 12(d) shows the resulting 50-s regionally averaged map obtained when a weighted average is applied to pixels within a 3° radius. By comparing Figs 12(c) and (d), one can see the influence of the averaging scheme on the regionally averaged map. For example, we typically do not see extreme $1/Q$ values in the areas where the individual attenuation values were masked out, as those pixels are (by design) heavily influenced by averaging of attenuation values from nearby pixels, which tends to drive the result towards an intermediate value. In Fig. 13 regionally averaged attenuation maps, constructed using the approach described above, are shown for four periods.

7 IMPLICATIONS FOR INTRINSIC SHEAR ATTENUATION

In this section we explore the continent-scale variations in intrinsic shear attenuation that are suggested by the regionally averaged attenuation maps described in the previous section. Development of a 3-D model of shear attenuation in the North American upper mantle is clearly an important goal of our work and yet one that cannot be fully realized at this stage, given the narrow range of periods (and therefore limited depth sensitivity) available. Furthermore, our approach for eliminating individual attenuation values that are contaminated by focusing effects is approximate and requires spatial averaging to fill the gaps left by the eliminated values, resulting in a relatively smooth model that likely underestimates the true range of attenuation variations. For these reasons, in this section we summarize the distribution of shear-attenuation values but do not show slices of the model.

The Rayleigh wave attenuation values Q^{-1} at latitude θ, longitude ϕ, and angular frequency ω in Fig. 13 are related to intrinsic bulk attenuation $Q_\kappa{}^{-1}(r, \theta, \phi)$ and shear attenuation $Q_\mu{}^{-1}(r, \theta, \phi)$ in

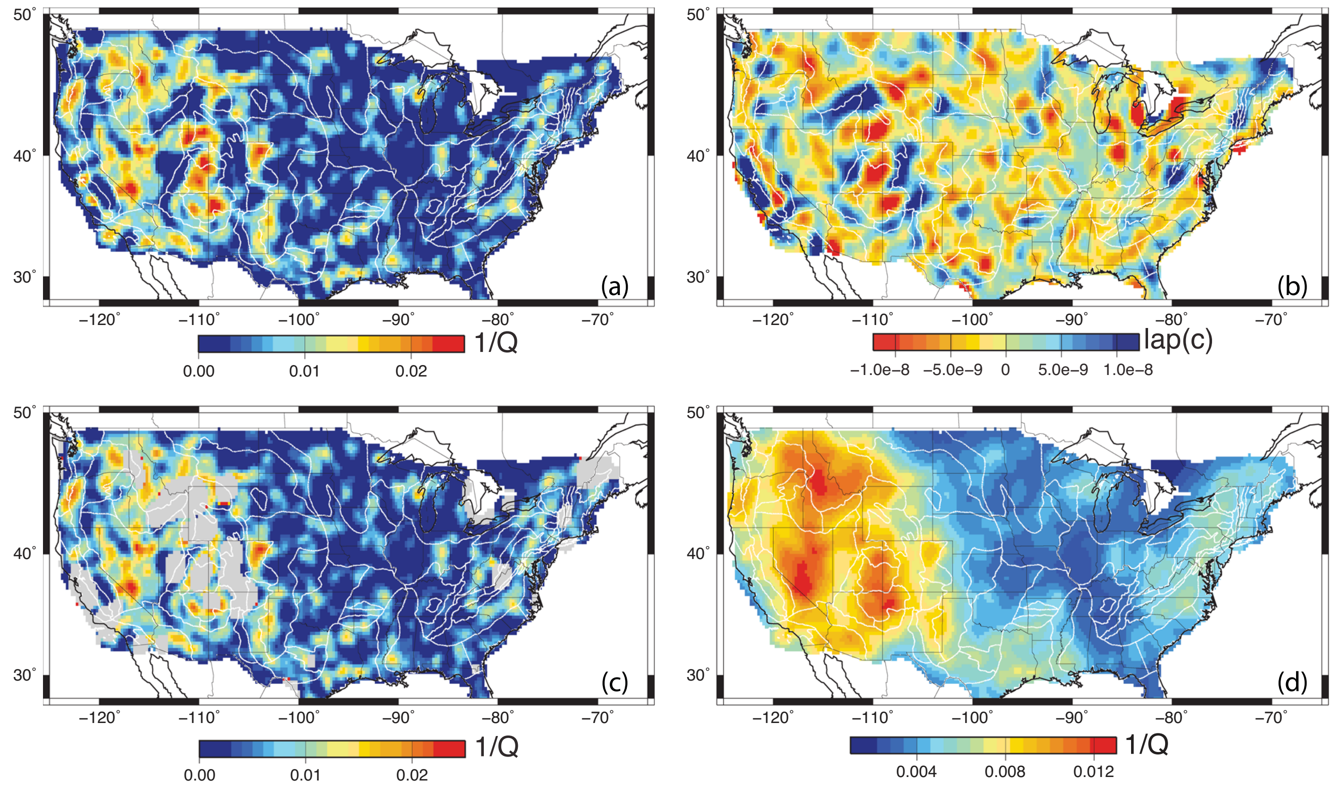

Figure 12. (a) 50-s Rayleigh wave attenuation determined from azimuthal-averaging approach applied to selected values of corrected amplitude decay (Fig. 9c). (b) Laplacian of the 50-s phase-velocity map; the phase-velocity map was filtered using a 400-km Gaussian filter prior to calculation of Laplacian. (c) As in (a) but pixels with absolute value of the Laplacian(c) $>5\times10^{-9}$ masked out (grey); lower and upper bounds of 1/600 and 1/30 have also been applied. (d) Final 50-s attenuation map determined from regional averaging of the attenuation values in (c). Average, weighted by distance, has been calculated from the individual attenuation values within radius $= 3^{\mathrm{o}}$.

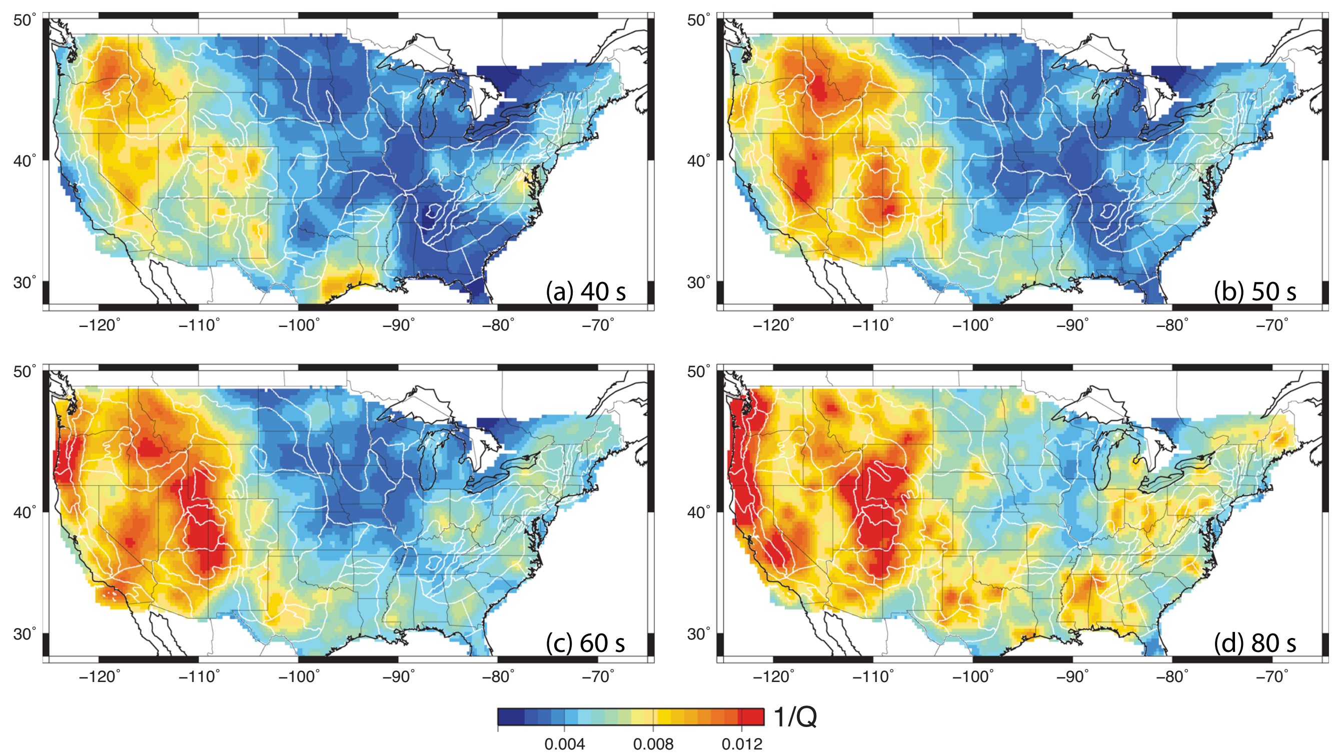

Figure 13. Regionally averaged Rayleigh wave attenuation maps at four periods.

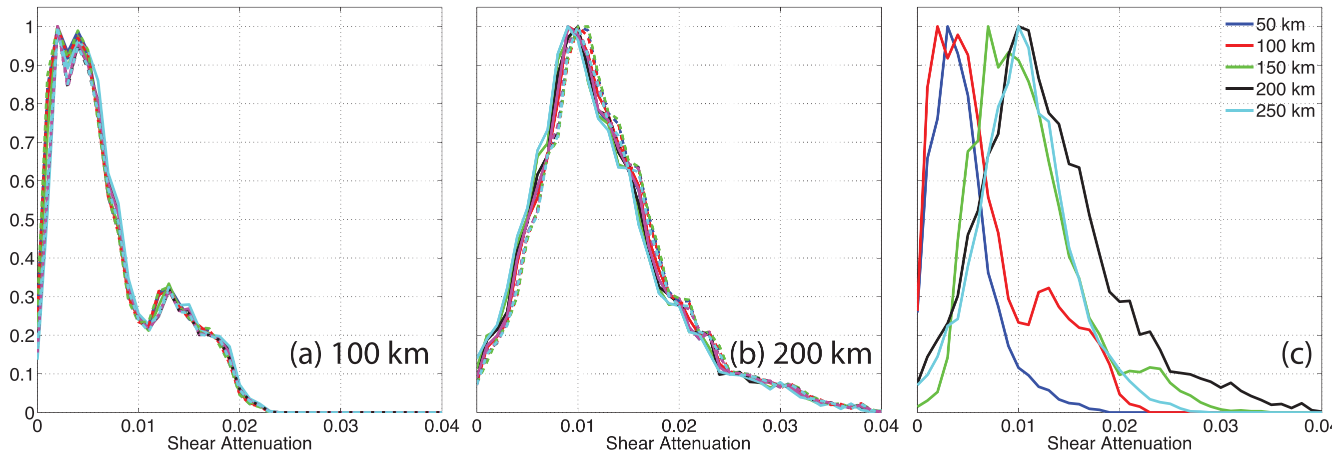

Figure 14. (a, b) Normalized histograms showing the distribution of shear-attenuation values in 14 003 pixels (0.25° spacing) at 100-km depth and 200-km depth. Results from twelve different model scenarios are shown. The solid and dashed lines correspond to parameterizations with the bottom of the model domain at depths of 400 and 300 km, respectively. Lin colours correspond to different assumptions about the $1/Q_\mu$ values prescribed at the top/bottom of the model: 300/133 (blue), 300/193 (red), 300/73 (green), 600/133 (black), 600/193 (magenta) and 600/73 (cyan). In many cases the lines plot on top of each other. (c) Normalized histogram of shear-attenuation values at five depths. Model scenario: 11 radial splines with $1/Q_\mu$ fixed to 1/300 at 0 km and 1/193 at 300 km.

Earth's crust and mantle through

$$Q^{-1}(\omega,\theta,\phi) = \int_0^{\alpha} \left[k(r)\, K_k(\omega,r)\, Q_k^{-1}(r,\theta,\phi) + \mu(r)\, K_\mu(\omega,r)\, Q_\mu^{-1}(r,\theta,\phi)\right] r^2 \mathrm{d}r, \qquad (14)$$

where integration over radius r proceeds from the center of the Earth to the surface (r = a), and $\kappa(r)K_\kappa(\omega, r)$ and $\mu(r)K_\mu(\omega, r)$ are the kernels that describe the radial sensitivity of Rayleigh waves to bulk and shear attenuation, respectively. Since $Q_\kappa{}^{-1} \ll Q_\mu{}^{-1}$ throughout the mantle (e.g. Durek & Ekström 1996; Resovsky *et al.* 2005) and the Rayleigh waves utilized in this study are much less sensitive to bulk attenuation than shear attenuation, we assume that $Q_\kappa{}^{-1} = 0$ and attribute all Rayleigh wave dissipation to shear attenuation.

We investigate the range of upper-mantle shear-attenuation values that are suggested by our regionally averaged attenuation maps by inverting the attenuation values in each pixel in the period range 40–80 s for shear attenuation. We calculate sensitivity kernels with PREM (Dziewonski & Anderson 1981) as the reference 1-D earth model, as has been done for global surface wave attenuation studies (e.g. Dalton *et al.* 2008). The model is parameterized vertically with radial splines. We experiment with 13 radial splines distributed from the surface to 400-km depth and 11 radial splines distributed from the surface to 300 km. In the horizontal directionthere are 14 003 pixels, spaced every 0.25°. Damping is used to control vertical smoothness, and we prescribe attenuation values at the top and bottom of the model domain. Attenuation at the surface (r = 6371 km) is assigned to be either 1/300 or 1/600 (e.g. Dziewonski & Anderson 1981; Durek & Ekström 1996). Attenuation at the bottom of the model (r = 6071 km or r = 5971 km) is assigned to be either 1/193, 1/133 or 1/73. All possible combinations of parameters and parameterizations are tested, resulting in twelve separate model scenarios. The relatively narrow range of periods used for this exploration of intrinsic attenuation (40–80 s) limits the depth sensitivity (∼40–200 km). By testing different parameterizations and prescribing different constraints at the top and bottom of the model, we are able to assess how sensitive our results are to these assumptions.

Figs 14(a) and (b) summarize the distribution of shear attenuation values obtained in the 14 003 pixels using a single damping parameter for twelve different model scenarios (i.e. distribution of radial splines and prescribed attenuation values at the top and bottom of the model). The various attenuation models are not very sensitive to assumptions about the model parameterization. At depths close to the top and bottom of the model domain, the models are more strongly dependent on the prescribed attenuation values. The two peaks in the distribution at 100-km depth are associated with the low-attenuation central and eastern United States and the high-attenuation western United States. At 200-km depth the continent is not so clearly divided into the high-attenuation west and low-attenuation east, which is reflected in the shape of the single-peaked histograms, although there is still a substantial tail of high-attenuation values. Fig. 14(c) summarizes the distribution of attenuation values across the continent from 50 to 250 km, though our data have little sensitivity to depths >200 km. In comparison to the doubly peaked histograms at 100 and 150 km, the histograms at 200 and 250 km are dominated by a single peak and are centred at slightly higher shear-attenuation values, consistent with the slightly higher average Rayleigh wave attenuation values that characterize the United States in the maps at 60 and 80 s relative to 40 and 50 s (Fig. 13). Fig. 14(c) suggests that the highest attenuation values are observed around 200-km depth and begin to decrease at greater depths, but inversions that use a broader range of frequencies will be needed to confirm this trend. Using a smaller (larger) value to control the vertical smoothness results in a slightly wider (narrower) range of values at each depth and a stronger (weaker) dependence of the result on whether the bottom of the model is located at 300 or 400 km.

The 3-D shear-attenuation values described in this section represent a preliminary model of the anelastic properties of the North American upper mantle. Future work will explore a better treatment for focusing effects, which will allow finer-scale attenuation structure to be investigated and a broader range of frequencies to be included.

8 CONCLUSIONS

We have used a new data set of Rayleigh wave amplitudes and traveltimes measured at USArray stations to solve for phase-velocity and attenuation maps at periods between 25 and 100 s. The phase-velocity maps show strong agreement with previously published maps for the North American upper mantle. The focus of this study is imaging variations in anelastic properties beneath North America; separating the effects of attenuation, focusing by elastic structure, and receiver site amplification is the primary challenge of this effort. In this study, it is assumed that the Laplacian of the observed traveltime field describes focusing effects, and we consider three different approaches for separating attenuation and site amplification, following the theory and approach described and applied to the western United States by Lin *et al.* (2012). The attenuation values determined with these three approaches contain the same first-order features: high attenuation in the western United States and low attenuation in the central and eastern United States, with slightly higher attenuation along the eastern seaboard.

The overall high attenuation in the west is interrupted in several places by extremely low-attenuation values. These low-attenuation zones are typically also associated with very low phase velocity; thus, we suspect that these zones are the result of inaccuracies in the treatment of focusing effects in areas with strong local variations in phase velocity. There are also areas of anomalously high attenuation, which are more difficult to recognize in the high-attenuation western United States. Given the 70-km spacing of USArray, simulating focusing effects using existing phase-velocity maps or 3-D velocity models for the region, rather than using the observed traveltime field, may ultimately prove to yield more accurate results. We show, using finite-difference wavefield simulations, that the magnitude of the Laplacian of the observed traveltime field depends on station spacing, especially in areas characterized by a large Laplacian amplitude. An additional factor that could introduce bias into our attenuation estimates is the approximation of the Rayleigh wave as a single-mode 2-D wave (e.g. eqs 1 and 2 and Lin *et al.* 2012). Yang & Forsyth (2006) showed with numerical simulations that 2-D single-scattering kernels do not accurately predict focusing effects in the immediate vicinity of a strong elastic anomaly due in large part to the assumption of isotropic scattering, which neglects the azimuthal dependence of scattering. The 2-D kernels perform much better when non-isotropic scattering is allowed. Accurate estimation of the relative contributions of forward- and back-scattering is especially important; this factor varies with depth, necessitating assumptions about the scattering radiation pattern when collapsing the 3-D sensitivity into two dimensions. Lin & Ritzwoller (2011b) have shown that unmodelled back-scattering can also introduce bias into estimates of azimuthal anisotropy.

Here we estimate those attenuation values likely more contaminated by unmodelled focusing effects by using the Laplacian of the phase-velocity map. Pixels with very large values of the Laplacian (positive or negative) are eliminated; we find a strong correspondence between the Laplacian of phase velocity and the anomalous attenuation values, which provides support for this approach. We then generate attenuation maps by performing a regional average of the values that remain after this selection process. The regionally averaged maps show high attenuation in the west that transitions to low attenuation beneath the central United States; the transition occurs fairly abruptly in the vicinity of the Rocky Mountain Front. Attenuation values along the east coast are intermediate between the extremes in the western and central United States.

Finally, we investigate the range of intrinsic shear-attenuation values that are suggested by the Rayleigh wave attenuation maps at periods between 40 and 80 s. These results suggest that the division of the continent into a high-attenuation western province and a low-attenuation eastern province disappears between 100- and 200-km depths. Smaller-scale variations in shear attenuation can be explored with more precise accounting for focusing effects in areas with large local gradients in elastic properties.

ACKNOWLEDGEMENTS

We thank Editor Gabi Laski, Fan-Chi Lin and an anonymous reviewer for their careful and constructive comments. We thank Celia Eddy and Göran Ekström for sharing their maps of location site amplification, and Fan-Chi Lin for providing FTAN measurements for comparison. We are grateful to everyone contributing the deployment and operation of the USArray Transportable Array. Seismic data were collected from the IRIS Data Management Center (DMC, www.iris.edu). The database of US physiographic boundaries (Vigil *et al.* 2000) was downloaded from water.usgs.gov/GIS/metadata/usgswrd/XML/physio.xml. The upper mantle shear velocity model CUB2.0 (Shapiro & Ritzwoller 2002) and WCUS_Shen_2012 (Shen *et al.* 2013) are downloaded from ciei.colorado.edu/∼nshapiro/MODEL/, for which we thank the authors of allowing those models publicly open. This work was supported by the U.S. National Science Foundation under Grants EAR-1444421 and EAR-1252069 to C.A.D.

REFERENCES

Abers, G.A., Fischer, K.M., Hirth, G., Wiens, D.A., Plank, T., Holtzman, B.K., McCarthy, C. & Gazel, E., 2014. Reconciling mantle attenuation-temperature relationships from seismology, petrology, and laboratory measurements, *Geochem. Geophys. Geosyst.,* **15,** 3521–3542.

Anderson, D.L., 1967. The anelasticity of the mantle, *Geophys. J. R. astr. Soc.,* **14,** 135–164.

Booth, C.M., Forsyth, D.W. & Weeraratne, D.S., 2014. Upper mantle Q structure beneath old seafloor in the western Pacific, *J. geophys. Res.,* **119,** 3448–3461.

Brocher, T.M., 2005. Empirical relations between elastic wave speeds and density in the Earth's crust, *Bull. seism. Soc. Am.,* **95,** 2081–2092.

Christensen, N.I. & Mooney, W.D., 1995. Seismic velocity structure and composition of the continental crust: a global view, *J. geophys. Res.,* **100,** 9761–9788.

Dalton, C.A. & Ekström, G., 2006a. Global models of surface-wave attenuation, *J. geophys. Res.,* **111,** B05317, doi:10.1029/2005JB003997.

Dalton, C.A. & Ekström, G., 2006b.Constraints on global maps of phase velocity from surface-wave amplitudes, *Geophys. J. Int.,* **167,** 820–826.

Dalton, C.A. & Faul, U.H., 2010. The oceanic and cratonic upper mantle: clues from joint interpretation of global velocity and attenuation models, *Lithos,* **120,** 160–172.

Dalton, C.A., Ekström, G. & Dziewoński, A.M., 2008. The global attenuation structure of the upper mantle, *J. geophys. Res.,* **113,** B09303, doi:10.1029/2007JB005429.

Dalton, C.A., Ekström, G. & Dziewonski, A.M., 2009. Global seismological shear velocity and attenuation: a comparison with experimental observations, *Earth planet. Sci. Lett.,* **284,** 65–75.

Dalton, C.A., Hjörleifsdóttir, V. & Ekström, G., 2013. A comparison of approaches to the prediction of surface wave amplitude, *Geophys. J. Int.,* **196,** 386–404.

Dunn, R.A. & Forsyth, D.W., 2003. Imaging the transition between the region of mantle melting and the crustal magma chamber beneath the southern East Pacific Rise with short-period Love waves, *J. geophys. Res.*, **108**(B7), 2352, doi:10.1029/2002JB002217.

Durek, J.J. & Ekström, G., 1996. A radial model of anelasticity consistent with long-period surface wave attenuation, *Bull. seism. Soc. Am.,* **86,** 144–158.

Dziewoński, A.M. & Anderson, D.L., 1981. Preliminary reference Earth model, *Phys. Earth planet. Inter.,* **25,** 297–356.

Eddy, C.L. & Ekström, G., 2014. Local amplification of Rayleigh waves in the continental United States observed on the USArry, *Earth planet. Sci. Lett.,* **402,** 50–57.

Ekström, G., 2014. Love and Rayleigh phase-velocity maps, 5–40 s, of the western and central USA from USArray data, *Earth planet. Sci. Lett.,* **402,** 42–49.

Ekström, G., Dalton, C.A. & Nettles, M., 2006. Observations of time-dependent errors in long-period instrument gain at global seismic stations, *Seismol. Res. Lett.,* **77,** 12–22.

Ekström, G., Nettles, M. & Dziewoński, A.M., 2012. The global CMT Project 2004–2010: centroid-moment tensors for 13 017 earthquakes, *Phys. Earth planet. Inter.,* **200–201,** 1–9.

Faul, U.H. & Jackson, I., 2005. The seismological signature of temperature and grain size variations in the upper mantle, *Earth planet. Sci. Lett.,* **234,** 119–134.

Faul, U.H., Gerald, J.D.F. & Jackson, I., 2004. Shear wave attenuation and dispersion in melt-bearing olivine polycrystals: 2. Microstructral interpretation and seismological implications, *J. geophys. Res.,* **109,** B06202, doi:10.1029/2003JB002407.

Gao, H. & Shen, Y., 2015. Validation of recent shear wave velocity models in the United States with full-wave simulation, *J. geophys. Res.,* **120,** 344–358.

Gee, L.S. & Jordan, T.H., 1992. Generalized seismological data functionals, *Geophys. J. Int.,* **111,** 363–390.

Goes, S., Govers, R. & Vacher, P., 2000. Shallow mantle temperature under Europe from P and S wave tomography, *J. geophys. Res.,* **105,** 11 153–11 169.

Gribb, T.T. & Cooper, R.F., 1998. Low-frequency shear attenuation in polycrystalline olivine: grain boundary diffusion and the physical significance of the Andrade model for viscoelastic rheology, *J. geophys. Res.,* **103,** 27 267–27 279.

Gung, Y. & Romanowicz, B., 2004. *Q* tomography of the upper mantle using three-component long-period waveforms, *Geophys. J. Int.,* **157,** 813–830.

Hammond, W.C. & Humphreys, E.D., 2000a. Upper mantle seismic wave velocity: effects of realistic partial melt geometries, *J. geophys. Res.,* **105,** 10 975–10 986.

Hammond, W.C. & Humphreys, E.D., 2000b. Upper mantle seismic wave attenuation: effects of realistic partial melt distribution, *J. geophys. Res.,* **105,** 10 987–10 999.

Hwang, Y.K., Ritsema, J. & Goes, S., 2009. Spatial variations of P wave attenuation in the mantle beneath North America, *J. geophys. Res.,* **114,** B06312, doi:10.1029/2008JB006091.

Jackson, I. & Faul, U.H., 2010. Grainsize-sensitive viscoelastic relaxation in olvine: towards a robust laboratory-based model for seismological application, *Phys. Earth. planet. Inter.,* **183,** 151–163.

Jackson, I., Gerald, J.D.F., Faul, U.H. & Tan, B.H., 2002. Grain-size sensitive seismic wave attenuation in polycrystalline olivine, *J. geophys. Res.,* **107,** 2360, doi:10.1029/2001JB001225.

Jackson, I., Faul, U.H., Gerald, J.D.F. & Tan, B.H., 2004. Shear-wave attenuation and dispersion in melt-bearing olivine polycrystals. I: Specimen fabrication and mechanical testing, *J. geophys. Res.,* **109,** B06201, doi:10.1029/2003JB002406.

Jin, G. & Gaherty, J.B., 2015. Surface wave phase-velocity tomography based on multichannel cross-correlation, *Geophys. J. Int.,* **201** (3), 1383–1398.

Kanamori, H. & Anderson, D.L., 1977. Importance of physical dispersion in surface wave and free oscillation problems: review, *Rev. Geophys. Space Phys.,* **15,** 105–112.

Karato, S., 1993. Importance of anelasticity in the interpretation of seismic tomography, *Geophys. Res. Lett.,* **20,** 1623–1626.

Karato, S., 2003. Mapping water content in the upper mantle, in *Inside the Subduction Factory,* Vol. 138, Geophys. Monogr. Ser., pp. 135–152, AGU.

Karato, D. & Jung, H., 1998. Water, partial melting and the origin of the seismic low velocity and high attenuation zone in the upper mantle, *Earth planet. Sci. Lett.,* **157,** 193–207.

Kennet, B.L.N., Engdahl, E.R. & Buland, R., 1995. Constraints on seismic velocites in the Earth from travel times, *Geophys. J. Int.,* **122**, 108–124.

Larson, E.W.F., Tromp, J. & Ekström, E., 1998. Effects of slight anisotropy on surface waves, *Geophys. J. Int.,* **132,** 654–666.

Lawrence, J.F., Shearer, P.M. & Masters, G., 2006. Mapping attenuation beneath North America using waveform cross-correlation and cluster analysis, *Geophys. Res. Lett.,* **33,** L07315, doi:10.1029/2006GL025813.

Lay, T. & Helmberger, D.V., 1981. Body wave amplitude patterns and upper mantle attenuation variations across North America, *Geophys. J. R. astr. Soc.,* **66,** 691–726.

Lay, T. & Wallace, T.C., 1988. Multiple ScS attenuation and travel times beneath western North America, *Bull. seism. Soc. Am.,* **78,** 2041–2061.

Lin, F.-C. & Ritzwoller, M.H., 2011. Helmholtz surface wave tomography for isotropic and azimuthally anisotropic structure, *Geophys. J. Int.,* **186,** 1104–1120.

Lin, F.-C., Ritzwoller, M.H. & Snieder, R., 2009. Eikonal tomography: surface wave tomography by phase front tracking across a regional broadband seismic array, *Geophys. J. Int.,* **177** (3), 1091–1110.

Lin, F.-C., Tsai, V.C. & Ritzwoller, M.H., 2012. The local amplification of surface waves: a new observable to constrain elastic velocities, density, and anelastic attenuation, *J. geophys. Res.,* **117,** B06302, doi:10.1029/2012JB009208.

Liu, H.P., Anderson, D.L.& & Kanamori, H., 1976. Velocity dispersion due to anelasticity: implications for seismology and mantle composition, *Geophys. J. R. astr. Soc.,* **47,** 41–58.

Mitchell, B.J., 1975. Regional Rayleigh wave attenuation in North America, *J. geophys. Res.,* **80,** 4904–4916.

Resovsky, J., Trampert, J. & Van der Hilst, R.D., 2005. Error bars for the global seismic Q profile, *Earth planet. Sci. Lett.,* **230,** 413–423.

Romanowicz, B. & Gung, Y., 2002. Superplumes from the core-mantle boundary to the lithosphere: implications for heat flux, *Science,* **296,** 513–516.

Roth, E.G., Wiens, D.A. & Zhao, D., 2000. An empirical relationship between seismic attenuation and velocity anomalies in the upper mantle, *Geophys. Res. Lett.,* **27,** 601–604.

Ruan, Y. & Zhou, Y., 2012. The effects of 3-D anelasticity (Q) structure on surface-wave amplitudes, *Geophys. J. Int.,* **189,** 967–983.

Rychert, C.A., Fischer, K.M., Abers, G.A., Plank, T., Syracuse, E., Protti, J.M., Gonzalez, V. & Strauch, W., 2008. Strong along-arc variations in attenuation in the mantle wedge beneath Costa Rica and Nicaragua, *Geochem. Geophys. Geosyst.,* **9,** Q10S10, doi:10.1029/2008GC002040.

Sato, H., Sacks, I.S. & Murase, T., 1989. The use of laboratory velocity data for estimating temperature and partial melt fraction in the low velocity zone: comparison with heat flow and electrical conductivity studies, *J. geophys. Res.,* **94,** 5689–5704.

Selby, N.D. & Woodhouse, J.H., 2000. Controls on Rayleigh wave amplitudes: attenuation and focusing, *Geophys. J. Int.,* **142,** 933–940.

Shapiro, N.M. & Ritzwoller, M.H., 2002. Monte Carlo inversion for a global shear velocity model of the crust and upper mantle, *Geophys. J. Int.,* **151,** 88–105.

Shapiro, N.M. & Ritzwoller, M.H., 2004. Thermodynamic constraints on seismic inversions, *Geophys. J. Int.,* **157,** 1175–1188.

Shen, W., Ritzwoller, M.H. & Schulte-Pelkum, V., 2013. A 3-D model of the crust and uppermost mantle beneath the central and western US by joint inversion of receiver functions and surface wave dispersion, *J. geophys. Res.,* **118,** 262–276.

Shito, A., Karato, S., Matsukage, K. & Nishihara, Y., 2006. Toward mapping water content, temperature and major element chemistry in Earth's upper mantle from seismic tomography, in *Earth's Deep Water Cycle,* Vol. 168, Geophys. Monogr. Ser., pp. 225–236, AGU.

Smith, W.H.F. & Wessel, P., 1990. Gridding with continuous curvature splines in tension, *Geophysics,* **55,** 293–305.

Stachnik, J.C., Abers, G.A. & Christensen, D.H., 2004. Seismic attenuation and mantle wedge temperatures in the Alaska subduction zone, *J. geophys. Res.,* **109,** B10304, doi:10.1029/2004JB003018.

Stixrude, L. & Lithgow-Bertelloni, C., 2005. Mineralogy and elasticity of the oceanic upper mantle: origin of the low-velocity zone, *J. geophys. Res.,* **110,** B03204, doi:10.1029/2004JB002965.

Sundberg, M. & Cooper, R.F., 2010. A composite viscoelastic model for incorporating grain boundary sliding and transient diffusion creep;

correlating creep and attenuation responses for materials with a fine grain size, *Phil. Mag.,* **90,** 20, 2817–2840.

Vigil, J.F., Pike, R.J. & Howell, D.G., 2000. A tapestry of time and terrain, Pamphlet to accompany, Geologic Investigations Series I-2720, U.S. Department of the Interior, U.S. Geological Survey.

Wang, Z. & Dahlen, F.A., 1994. JWKB surface-wave seismograms on a laterally heterogeneous Earth, *Geophys. J. Int.,* **119,** 381–401.

Wang, Z. & Dahlen, F.A., 1995. Validity of surface-wave ray theory on a laterally heterogeneous Earth, *Geophys. J. Int.,* **123,** 757–773.

Wei, S.S., Wiens, D.A., Zha, Y., Plank, T., Webb, S.C., Blackman, D.K., Dunn, R.A. & Conder, J.A., 2015. Seismic evidence of effects of water on melt transport in the Lau back-arc mantle, *Nature,* **518**, 395–398.

Wiens, D., Conder, J. & Faul, U., 2008. The seismic structure and dynamics of the mantle wedge, *Annu. Rev. Earth planet. Sci.,* **36,** 421–455.

Woodhouse, J.H. & Wong, Y.K., 1986. Amplitude, phase and path anomalies of mantle waves, *Geophys. J. R. astr. Soc.,* **87,** 753–773.

Yang, Y. & Forsyth, D.W., 2006. Rayleigh wave phase velocities, small-scale convection, and azimuthal anisotropy beneath southern California, *J. geophys. Res.,* **111,** B07306, doi:10.1029/2005JB004180.

Yang, Y. & Forsyth, D.W., 2008. Attenuation in the upper mantle beneath Southern California: physical state of the lithosphere and asthenosphere, *J. geophys. Res.,* **113,** B033308, doi:10.1029/2007JB005118.

Yang, Y., Forsyth, D.W. & Weeranratne, D.S., 2007. Seismic attenuation near the East Pacific Rise and the origin of the low-velocity zone, *Earth planet. Sci. Lett.,* **258,** 260–268.

Zhang, W., Shen, Y. & Zhao, L., 2012. Three-dimensional anisotropic seismic wave modeling in spherical coordinate by a collocated-grid finite difference method, *Geophys., J. Int.,* **188,** 1359–1381.

Zhu, H., Bozdağ, E., Duffy, T.S. & Tromp, J., 2013. Seismic attenuation beneath Europe and the North Atlantic: implications for water in the mantle, *Earth planet. Sci. Lett.,* **381,** 1–11.